BIOCHEMISTRY
including biophysical chemistry & molecular biology

Article

pubs.acs.org/biochemistry

Mössbauer Study and Modeling of Iron Import and Trafficking in Human Jurkat Cells

Nema D. Jhurry,[†] Mrinmoy Chakrabarti,[‡] Sean P. McCormick,[‡] Vishal M. Gohil,[†] and Paul A. Lindahl*[,†,‡]

[†]Department of Biochemistry and Biophysics, Texas A&M University, College Station, Texas 77843-2128, United States

[‡]Department of Chemistry, Texas A&M University, College Station, Texas 77843-3255, United States

Ⓢ *Supporting Information*

ABSTRACT: The Fe content of Jurkat cells grown on transferrin-bound iron (TBI) and Fe^{III} citrate (FC) was characterized using Mössbauer, electron paramagnetic resonance, and UV−vis spectroscopies, as well as electron and inductively coupled plasma mass spectrometry. Isolated mitochondria were similarly characterized. Fe-limited cells contained ~100 μM essential Fe, mainly as mitochondrial Fe and nonmitochondrial non-heme high-spin Fe^{II}. Cells replete with Fe also contained ferritin-bound Fe and Fe^{III} oxyhydroxide nanoparticles. Only 400 ± 100 Fe ions were loaded per ferritin complex, regardless of the growth medium Fe concentration. Ferritin regulation thus appears to be more complex than is commonly assumed. The magnetic and structural properties of Jurkat nanoparticles differed from those of yeast mitochondria. They were smaller and may be located in the cytosol. The extent of nanoparticle formation scaled nonlinearly with the concentration of Fe in the medium. Nanoparticle formation was not strongly correlated with reactive oxygen species (ROS) damage. Cells could utilize nanoparticle Fe, converting such aggregates into essential Fe forms. Cells grown on galactose rather than glucose respired faster, grew slower, exhibited more ROS damage, and generally contained more nanoparticles. Cells grown with TBI rather than FC contained less Fe overall, more ferritin, and fewer nanoparticles. Cells in which the level of transferrin receptor expression was increased contained more ferritin Fe. Frataxin-deficient cells contained more nanoparticles than comparable wild-type cells. Data were analyzed by a chemically based mathematical model. Although simple, it captured essential features of Fe import, trafficking, and regulation. TBI import was highly regulated, but FC import was not. Nanoparticle formation was not regulated, but the rate was third-order in cytosolic Fe.

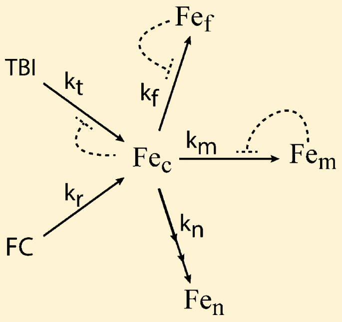

Iron is essential in human metabolism because of its extensive redox, substrate binding, and catalytic properties. This transition metal is found in various forms, including hemes, Fe−S clusters, and non-heme mononuclear and binuclear centers. Conversely, excess Fe is widely regarded to be toxic to cells because it can generate reactive oxygen species (ROS) through the Fenton reaction.[1] Hence, Fe import, trafficking, utilization, and storage must be tightly regulated by cells.[2,3]

Mammalian cells import Fe through many pathways, the best studied of which involves transferrin, a blood plasma protein that coordinates two Fe^{III} ions.[4] The cell-surface transferrin receptor TfRC1 mediates the endocytic import of transferrin-bound iron (TBI). This is followed by acidification of the endosome, release of Fe^{III} from transferrin, reduction to Fe^{II}, and export of Fe^{II} from the endosome to the cytosol via the divalent metal transporter DMT1.[5] Expression of the transferrin receptor (TfRC1) is regulated post-transcriptionally by iron regulatory proteins IRP1 and IRP2.[6] Both bind to and stabilize the 3′-UTR of TfRC1 mRNA under iron-deficient conditions. This promotes TfRC1 translation and thus Fe import via the TBI pathway.[6]

IRP1 and IRP2 also regulate the concentration of ferritin in the cell. Ferritin is a spherical 24-subunit protein complex used by the cell to store Fe. It has a hollow 7 nm diameter core that can store up to ~4500 Fe^{III} ions as an oxyhydroxide aggregate.[7] When cells are iron-deficient, IRP1 and IRP2 bind to the 5′-UTR of ferritin mRNA. This prevents mRNA translation and leads to a decline in the level of ferritin expression. When cells are replete with Fe, IRP1 and IRP2 do not bind ferritin mRNA, which increases the level of ferritin expression, allowing storage of excess cellular Fe.[6]

Other Fe import pathways are less well-defined and are often termed a single pathway in which non-transferrin-bound iron (NTBI) is imported.[8] Fe^{III} citrate (FC) is a likely component of NTBI.[9,10] Although many important aspects of NTBI and its import pathways are known, much remains to be learned regarding their role in cellular physiology. A cell-surface ferrireductase is required for the reduction of NTBI Fe^{III} to Fe^{II} prior to uptake.[11] Cell-surface metal transporters such as DMT1,[12] zinc transporter ZIP14,[13] Dcytb, and L-type calcium channels[14] may be involved. NTBI may also be imported via bulk and/or adsorptive endocytosis.[15]

Although incompletely defined, NTBI plays important roles in a number of diseases. NTBI is found in the blood plasma of patients with Fe overload diseases such as β-thalassemia,[16] idiopathic hemochromatosis,[17] hypotransferrinemia,[18] and

Received: July 26, 2013
Revised: September 21, 2013
Published: November 1, 2013

hereditary hemochromatosis.[19] This typically leads to the accumulation of iron in the liver and/or spleen. NTBI has also been implicated in the pathology of Alzheimer's disease.[20] NTBI uptake is not as tightly controlled as that of TBI, consistent with a role in cellular Fe overload and Fe-induced toxicity.[8] Hepatocytes import NTBI >20-fold faster than they import TBI,[21] which explains why NTBI is cleared efficiently from the blood by the liver.[22] Growth of cells on NTBI leads to severe Fe overload and oxidative damage.[23−25]

Few studies have probed Fe metabolism in human cells using iron-centric methods such as Mössbauer (MB) spectroscopy. This technique, used in conjunction with EPR and other biophysical methods (e.g., UV−vis and EM), can effectively evaluate the speciation of Fe in cells,[26−28] including human Jurkat cells grown in medium containing 10 μM FC.[28] The majority of Fe in these Fe-replete cells is bound to ferritin. Also evident are [Fe_4S_4] clusters and heme centers primarily associated with mitochondrial respiratory complexes, and Fe^{III} oxyhydroxide nanoparticles that exhibit superparamagnetic behavior.[28] In low-temperature low-field MB spectra, these nanoparticles exhibit a broad quadrupole doublet with a δ of 0.48 mm/s and a ΔE_Q of 0.57 mm/s.

Whitnall et al.[29] recently used MB spectroscopy to identify non-ferritin mitochondrial Fe deposits in a mouse model of Friedreich's ataxia. Friedreich's ataxia is the most common autosomal recessive ataxia; it causes progressive degeneration of the nervous system and heart. The deposits observed in heart tissue exhibit a broad quadrupole doublet in low-temperature low-field MB spectra. The associated parameters (δ = 0.48 mm/s, and ΔE_Q = 0.71 mm/s) are similar to those observed in Jurkat cells.[28] The mice had a muscle creatine kinase conditional knockout of frataxin, a mitochondrial matrix protein involved in Fe−S cluster biosynthesis.[30] Yeast lacking the frataxin homologue (Yfh1p) accumulate massive amounts of Fe^{III} phosphate oxyhydroxide nanoparticles in their mitochondria, along with a deficiency of Fe−S clusters and heme centers.[31]

Here, we report how the cellular concentrations of such Fe-containing species in human Jurkat cells vary with the concentration of FC and TBI in the growth medium. We examined the effect of different carbon sources (glucose vs galactose) on the Fe content of these cells and the effect of altering the expression levels of the transferrin receptor and frataxin. A mathematical model defining the fate of Fe that enters the cell as TBI and FC was developed.

■ EXPERIMENTAL PROCEDURES

Cell Culture. T-REx Jurkat cells (Life Technologies) were grown in a 24 L custom-designed all-glass bioreactor.[28] Cells were counted, and viability was evaluated as described previously.[28] Glucose-free RPMI 1640 custom-formulated powder (Gemini Bio-Products, West Sacramento, CA) was reconstituted in distilled, deionized water by following the manufacturer's instructions and supplementing with glucose or galactose (final concentration of 10 mM). The medium was also supplemented with $^{57}Fe^{III}$ citrate (^{57}FC) to final concentrations of 3, 10, and 30 μM. Aqueous $^{57}Fe^{III}$ was obtained by dissolving ^{57}Fe metal (Isoflex USA) in a 1:1 mixture of trace-metal-grade HNO_3 and HCl. The solution was diluted to a ^{57}Fe concentration of 80 mM with double-distilled and deionized (DDDI) H_2O to prepare a stock solution of ^{57}Fe. ^{57}FC was prepared by mixing the stock solution with DDDI H_2O, and adding sodium citrate dihydrate to a 4:1 molar ratio with ^{57}Fe. The pH of the solution was adjusted to 5.0, and the volume was adjusted with DDDI H_2O to afford a final concentration of 40 mM ^{57}FC. Enriched diferric transferrin (^{57}TBI) was prepared as described.[32] Apo-transferrin (Lee Biosolutions, St. Louis, MO) was dissolved at 10 mg/mL in phosphate-buffered saline [PBS (pH 7.4)] containing 0.01 M $NaHCO_3$. Four molar equivalents of ^{57}FC was added per mole of apo-transferrin. After 4 h at room temperature, the solution was centrifuged through a 20 kDa molecular mass cutoff membrane (Amicon Ultra 15 mL Concentrator). The ^{57}TBI-containing retentate (∼1 mL) was washed twice with 10 mL of PBS buffer containing 0.01 M $NaHCO_3$, spun through the 20 kDa cutoff membrane, and resuspended in PBS buffer at a concentration of 10 mg/mL. This ^{57}TBI stock was added to the cell culture medium to final concentrations of 3, 10, and 30 μM. Whole cell MB and EPR samples were prepared as described.[28]

Total RNA Isolation and cDNA Synthesis. Total RNA was extracted from Jurkat cells using the hot-phenol method.[27] Cells were grown to their maximal density (∼2.5 × 10^6 cells/mL) in 200 mL of culture medium and harvested by centrifugation at 700*g* for 5 min. Cells were washed twice with PBS buffer, resuspended in 2 mL of AE buffer [50 mM sodium acetate (pH 5.3) and 10 mM EDTA], and lysed via addition of SDS [final concentration of 1% (w/v)]. An equal volume of AE-saturated phenol was added to the cell lysate. The mixture was incubated at 65 °C for 10 min, vortexing every 2 min. The mixture was chilled rapidly in liquid N_2 and spun at 4000*g* for 5 min (Beckman Coulter) to separate the phases. The aqueous phase was collected, mixed thoroughly with an equal volume of a phenol/chloroform/isoamyl alcohol solution (25:24:1 volume ratio), and spun at 4000*g*. The aqueous phase was collected and mixed with 0.1 volume of 3 M sodium acetate and 2.5 volumes of pure ethanol. The solution was spun at 6400 rpm on a Qualitron DW-41 microcentrifuge for 5 min. The RNA-containing pellet was washed three times with 80% ethanol, air-dried for 1 h, and resuspended in 200 μL of TE buffer [10 mM Tris (pH 7.5) and 1 mM EDTA]. Contaminating DNA was removed using the DNA-Free reagent kit (Ambion) by following the manufacturer's instructions. cDNA was synthesized from RNA using the Super-Script Vilo cDNA synthesis kit (Applied Biosystems) by following the manufacturer's instructions.

TfRC1 Overexpression. Primers for cDNA amplification of the ORF of the TfRC1 gene were custom-designed (Life Technologies; forward primer, 5′-CACCATGATGGATCAAGCTAGATCAGC-3′; reverse primer, 5′-TTAAAACTCATTGTCAATGTCCCA-3′). Underlined nucleotides were added to the 5′ end of the forward primer to allow directional cloning into the pcDNA 3.1 vector (Life Technologies). The TfRC1 gene was amplified from the cDNA using Accuprime Supermix (Life Technologies), along with 300 nM forward and reverse primers, by following the manufacturer's instructions. Polymerase chain reaction (PCR) product size was determined by electrophoresis at 50 V using a 0.7% agarose gel and visualized using SYBR Green Fluorescent dye. The PCR product was sequenced using three sets of forward and reverse primers that were complementary to three adjacent 800 bp regions of the TfRC1 cDNA ORF sequence. Each 800 bp region was amplified via sequencing PCR, using the BigDye Terminator mix (Life Technologies), by following the manufacturer's instructions. PCR products were sequenced and analyzed on an ABI PRISM 3100 Genetic Analyzer. The TfRC1 PCR product was directionally cloned into the pcDNA 3.1 vector by following the manufacturer's instructions (Life Technologies). The resulting plasmid was transformed into OneShot TOP10 *Escherichia coli* competent cells (Life Technologies), which were then plated and grown at 37 °C overnight on LB agar plates containing 100 μg/mL ampicillin. A colony was picked from the plate and grown overnight in liquid LB containing 100 μg/mL ampicillin. Plasmids were purified from these *E. coli* cells using the PureLink Quick Plasmid Miniprep kit (Life Technologies) by following the manufacturer's instructions. The insertion of the TfRC1 gene into the plasmid was verified by performing PCR on the isolated plasmid using the forward and reverse primers (T7 forward and BGH reverse) provided with the pcDNA 3.1 Directional TOPO expression kit (Life Technologies). The sequence of the product cloned into the isolated plasmid was verified as described above.

Cells were transfected with the TfRC1 plasmid using Lipofectamine 2000 (Life Technologies) by following the manufacturer's instructions. Transfected cells were selected by growth for 2 weeks on medium containing 1000 μg/mL Geneticin. TfRC1 overexpression was verified by Western blotting, using a rabbit anti-TfRC1 primary antibody (Santa Cruz Biotechnology) and an HRP-conjugated anti-rabbit secondary antibody (Life Technologies).

For the iron starvation experiment, cells were first grown in 500 mL of medium to a density of 2×10^6 cells/mL, then spun down and washed once with sterile PBS containing 1 mM EGTA, and then suspended in neat sterile PBS buffer. The cells were spun down again and resuspended in complete unsupplemented medium containing 100 μM desferrioxamine for 12 h. The cells were pelleted again, washed with sterile neat PBS buffer, and resuspended again in 1500 mL of complete growth medium supplemented with 3 μM ^{57}TBI. Cells were grown to a maximal density of 3×10^6 cells/mL, and a MB sample was prepared as described previously.[28]

Isolation of Mitochondria. Mitochondria were isolated anaerobically from cells grown with 3 and 30 μM FC, as well as from cells grown with 1.5 μM diferric transferrin (i.e., 3 μM TBI) as described previously.[28] Freshly harvested cells were imported into an Ar atmosphere glovebox (MBraun, Labmaster, with <10 ppm O_2). They were washed twice with PBS buffer (pH 7.4) and then resuspended in degassed mitochondria isolation buffer {MIB [225 mM D-mannitol, 75 mM sucrose, 5 mM HEPES, 1 mM EGTA, and 1 mM PMSF (pH 7.4)]}. The cell suspension was subjected to N_2 cavitation at 800 psi for 15−20 min using a disruption vessel (model 4635, Parr instruments). The cavitation extract was centrifuged at 800*g* for 10 min. The resulting supernatant was centrifuged at 9000*g* for 30 min. The pellet was resuspended in MIB buffer, and the resulting solution was layered over a discontinuous gradient of 7.5 mL of 6% Percoll, 3 mL of 17% Histodenz, and 3 mL of 35% Histodenz in MIB as described previously.[33] The gradients were centrifuged at 45000*g* for 1 h. Mitochondria were collected at the 17%−35% interface, washed once with MIB, packed into MB cups or EPR tubes at 9000*g*, frozen, and stored in liquid N_2.

Quantitative Western Blots. Whole cell samples were packed into EPR tubes and diluted with a known volume of cell lysis buffer [0.1 M Tris-HCl buffer (pH 7.4) containing 1% Triton X-100 and 1 mM PMSF]. Protein concentrations were determined using the BCA Protein Assay kit (Thermo Scientific Pierce Protein Research Products). Various known amounts of human holo-ferritin (Lee Biosolutions) were loaded and separated on a 7.5% polyacrylamide native gel, along with 20 μL of cell lysates from cells grown in glucose- or galactose-containing medium supplemented with 3, 10, or 30 μM FC or TBI. Proteins were transferred to Immun-Blot PVDF membranes (Bio-Rad) overnight at 40 V. Membranes were treated for 2 h with a Blocker casein solution (Thermo Scientific) and then incubated for 1 h with a rabbit polyclonal primary antibody specific to mammalian ferritin (Abnova) diluted 1:200 in a Blocker casein solution. Membranes were then incubated with a goat anti-rabbit HRP conjugated secondary antibody (Life Technologies) diluted 1:3000 in a Blocker casein solution, followed by detection using the Thermo Scientific Enhanced Chemiluminescent Western Blotting substrate. Images were acquired using the FujiFilm LAS-4000 mini imager. Ferritin bands were analyzed using MultiGauge. A calibration curve was generated using the intensities of the human holo-ferritin bands. Ferritin concentrations of various cell lysates were quantified in terms of absolute cellular concentrations by accounting for the dilution factors and employing the packing efficiency of Jurkat cells that was determined previously.[28]

Biophysical Studies. EPR spectra of whole cells and isolated mitochondria were acquired using an X-band EMX spectrometer (Bruker Biospin Corp., Billerica, MA) equipped with an Oxford Instruments ER900A cryostat. Spin quantifications were performed with SpinCount (http://www.chem.cmu.edu/groups/hendrich/facilities/index.html), using 1.00 mM $CuSO_4$-EDTA as a standard. MB spectra were collected on a model MS4 WRC spectrometer and a model LHe6T spectrometer, capable of generating 0−6 T fields (SEE Co., Edina, MN). Both instruments were calibrated using the spectrum of α-Fe foil collected at room temperature.

For UV−visible spectroscopy, packed whole cell and mitochondrial samples from EPR tubes were diluted 2-fold with PBS buffer and MIB buffer, respectively, in the glovebox. They were placed in a custom 2 mm path length quartz UV−vis cuvette (Precision cells), sealed with a rubber septum, and removed from the box. Spectra were recorded on a Hitachi U3310 spectrometer with a Head-on photomultiplier tube. Heme signals were simulated using OriginPro as described previously.[34]

Ferritin Loading with Fe^{II} Sulfate in Whole Cell Lysates. After MB spectra of Jurkat cells grown with 30 μM ^{57}FC had been collected, the sample was thawed at room temperature and resuspended homogeneously in an equal volume of nondenaturing cell lysis buffer containing 1 mM PMSF. The lysate was split into two; to half was added $^{56}Fe^{II}$ sulfate in an aqueous solution to a final concentration of ∼6.25 mM, and the other half was left untreated. Both samples were exposed to air and mixed regularly for 2 h. Each sample was placed in a 3 mL MB cup and frozen immediately in liquid N_2.

Electron Microscopy and EDX Imaging. Cells were pelleted at 700*g* for 10 min and washed three times with RPMI 1640 medium. Cells were fixed overnight with acrolein vapor, dehydrated for 2 days with ethylene glycol, infiltrated, and embedded in epoxy resin by polymerization at 60 °C overnight. Ultrathin sections were obtained using an Ultracut E microtome (Reichert-Jung). Sections were carbon-stabilized overnight. Elemental analysis was performed on a TECNAI F20 Twin (scanning) transmission electron microscope [(S)TEM] fit with a Schottky field emission gun, a high-angle annular dark field (HAADF) detector, and an Oxford instruments ultrathin window energy-dispersive X-ray spectroscopy (EDX) detector. EDX spectra were collected at an ∼15° tilt angle with a stationary electron probe in STEM mode. The STEM was operated at an accelerating voltage of 200 kV. Spectral images were obtained from areas of interest by the electron microscope spectroscopy system. Elemental maps were acquired after choosing proper energy windows for element-specific transitions along with STEM−HAADF images.

Extracellular Flux Measurements. Cells were grown in RPMI 1640 medium containing 10 mM glucose or galactose, 5% newborn calf serum (Invitrogen), 10 μM FC, 100 units/L penicillin, 100 μg/L streptomycin, and 0.25 μg/L amphotericin B. Cells were spun at 700*g* for 5 min, and the pellet was washed with PBS buffer (pH 7.4). Cells were resuspended in Modified DMEM XF Assay Medium (Seahorse Biosciences, Billerica, MA) supplemented with either 10 mM glucose or 10 mM galactose. Cell-Tak (BD Biosciences), a cell and tissue adhesive, was diluted in 0.1 M sodium bicarbonate buffer (pH 8.0) by following the manufacturer's instructions. Fifty μL of the diluted (80 ng/μL) Cell-Tak solution were added to each well of a 24-well plate (Seahorse). O_2 consumption rate (OCR) and extracellular acidification rate (ECAR) were measured on the Extracellular Flux Analyzer (XF24) (Seahorse Biosciences) as described[35] with minor modifications. Briefly, Jurkat cells were seeded in Cell-Tak-treated XF24 well cell culture microplates at a density of 250000 cells/well in 10 mM glucose- or 10 mM galactose-containing XF assay medium and incubated at 37 °C for ~1 h prior to measurements. The baseline was measured three times prior to the addition of oligomycin (final concentration of 1 μM); the data presented here represent the third measurement. Each measurement included a mix (2 min), wait (3 min), and measure (2 min) cycle.

Oxyblot Assays. Whole cell lysates were prepared in cell lysis buffer (0.1 M Tris-HCl, 1% Triton X-100, and 1 mM PMSF). Twenty micrograms of cellular protein from each extract was solubilized with 10% (w/v) SDS, derivatized with 2,4-dinitrophenylhydrazine (DNPH), and loaded onto a 12% sodium dodecyl sulfate−polyacrylamide gel electrophoresis (SDS−PAGE) gel. Oxyblot analysis was performed using the DNPH primary antibody and the HRP-conjugated secondary antibody provided with the manufacturer's kit (Millipore).

Inductively Coupled Plasma Mass Spectrometry (ICP-MS). Packed whole cells and mitochondrial samples from EPR tubes were diluted with a known volume of PBS buffer and MIB buffer, respectively. Suspensions were digested overnight with concentrated trace-metal-grade nitric acid (final concentration of 20−30%) in 15 mL plastic screw-top tubes (BD Falcon). Digested samples were diluted with 4 mL of double-distilled and deionized water. Metal concentrations were measured in H_2 and He collision modes using ICP-MS (Agilent Technologies model 7700x). The absolute metal concentrations in the samples were obtained by adjusting for dilution factors and packing efficiencies and then averaging individual numbers.

Frataxin Knockdown. Frataxin protein knockdown was performed using the BLOCK-iT Inducible H1 RNAi Entry Vector kit (Life Technologies) by following the manufacturer's instructions. Four DNA oligonucleotide sequences encoding shRNA sequences specific to frataxin mRNA were designed using Life Technologies' BLOCK-iT RNAi Designer (rnaidesigner.invitrogen.com/rnaiexpress/) and cloned into the pENTR/H1/TO vector (Life Technologies). The plasmids were separately transformed into One Shot TOP10 chemically competent *E. coli* cells, which were plated and selected on LB agar plates with 50 μg/mL kanamycin. Bacterial colonies were picked and grown in liquid LB with 50 μg/mL kanamycin. Plasmids were purified from the liquid cultures using the PureLink HQ Mini Plasmid Purification Kit (Life Technologies) by following the manufacturer's instructions. Plasmids were transfected into Jurkat cells using the Xfect transfection reagent (Clontech) by following the manufacturer's instructions. Cells were grown under selection for 2−3 weeks in RPMI-1640 medium supplemented with tetracycline-negative fetal bovine serum (PAA Laboratories), 10 μg/mL blasticidin, and 50 μg/mL Zeocin. After selection, frataxin knockdown was induced by adding tetracycline to a final concentration of 3 μg/mL to the cultures. Transfected cells were allowed to grow in the presence of tetracycline for 4−5 days before being assayed for frataxin knockdown.

To assay for frataxin knockdown, transfected cells (both uninduced and induced) were grown to a maximal density of 2 × 10^6 cells/mL. Cells were spun down, washed with PBS buffer, and lysed using ice-cold RIPA buffer {radioimmunoprecipitation assay buffer [50 mM Tris-HCl, 150 mM NaCl, 1% Triton X-100, 0.5% sodium deoxycholate, and 0.1% SDS (pH 8.0)]}. Protein concentrations of cell lysates were determined using the Pierce BCA Protein Assay Kit (Thermo Fisher Scientific) by following the manufacturer's instructions. Forty micrograms of protein were boiled with denaturing Laemmli buffer and loaded on a 10% polyacrylamide gel. SDS−PAGE was conducted at 100 V, and proteins were transferred to Immunblot-PVDF membranes for 16 h at 20 V. Membranes were blocked for 2 h using a Blocker casein solution (Thermo Fisher Scientific). Membranes were then incubated (while being shaken) in rabbit polyclonal anti-frataxin primary antibody (Abcam) diluted 1:500 in PBS buffer. Membranes were subsequently rinsed three times with PBS buffer and incubated with goat anti-rabbit HRP-conjugated secondary antibody diluted 1:3000 in PBS buffer. Membranes were again rinsed three times with PBS buffer and immersed in Pierce ECL Western Blotting substrate (Thermo Fisher Scientific). Frataxin bands were detected using a FujiFilm LAS-4000 mini imager. The frataxin band intensities were analyzed by densitometry using ImageJ software. The DNA oligonucleotide encoding shRNA sequence 5′-GGACTATGATGTCTCTTTGG**CGAAC**CAAAGGAGACATCATA-3′ (loop region shown in bold), which targets bases 583−603 of frataxin mRNA, resulted in 50−70% knockdown of the frataxin protein after induction by tetracycline for 4−5 days, as judged by densitometry analysis of frataxin bands. The other shRNA sequences tested did not result in measurable frataxin knockdown. Therefore, the cells expressing the shRNA targeted to bases 583−603 were chosen for further analysis.

For spectroscopic investigations, transfected cells expressing shRNA targeted to frataxin were grown up to 3 L in complete RPMI-1640 medium supplemented with 50 μg/mL Zeocin and 10 μg/mL tetracycline to ensure continuous frataxin knockdown. ^{57}FC was added to a final concentration of 10 μM to the cell culture. Cells were washed with PBS containing 1 mM EGTA, followed by PBS without EGTA. Cells were then packed into MB cup and frozen in liquid N_2. After MB analysis, cells were thawed and analyzed by UV−vis spectroscopy and ICP-MS as described above. Wild-type (WT) cells grown with 10 μM ^{57}FC were analyzed alongside the transfected cells for comparison.

■ RESULTS

In this study, we used biophysical spectroscopy to characterize the iron content of human Jurkat cells grown under different conditions and genetically modified in different ways. For ease of discussion, we introduce the nomenclature #AB to describe the investigated states of WT cells. Accordingly, "#" indicates the concentration of Fe supplementing the growth medium, with possible values of 0, 3, 10, 30, or 100 μM. "A" indicates whether the supplemented Fe was TBI (A = T) or FC (A = F). "B" indicates whether the medium used glucose (B = U) or galactose (B = L) as the carbon source. For example, 3FU refers to cells grown on glucose-containing medium supplemented with 3 μM ferric citrate.

Iron Content of 3FU Cells. To evaluate the essential Fe content of human cells, we prepared cells under Fe-limited conditions. However, the concentration of natural abundance endogenous Fe in the medium was substantial (~6 μM[28]). Unlike yeast cells that can be grown in chemically defined minimal synthetic medium, human cells require fetal bovine or newborn calf serum, which contains significant amounts of Fe. Grown in such unsupplemented medium, Jurkat cells contained 100 ± 20 μM Fe. These cells grew at approximately the same rate as in medium supplemented with 3−30 μM ^{57}FC, namely with a doubling time (DT) of 24 h. This indicates that growth was not limited by the endogenous Fe content of the unsupplemented medium.

We attempted to decrease the concentration of endogenous Fe by adding (in different batches) desferrioxamine (DFO) and bathophenanthroline sulfonate (BPS), well-known chelators of Fe^{III} and Fe^{II} ions, respectively. Similar procedures have been used to create Fe-deficient conditions in yeast.[26] However, Jurkat cells did not grow in the presence of 100 μM DFO or BPS, which disallowed further analysis of cells subjected to Fe-deficient conditions.

For MB studies, we grew cells in medium supplemented with as little as 3 μM ^{57}FC. Although not strictly Fe-deficient, this Fe concentration was significantly lower than that used in our previous investigation.[28] The 5 K, 0.05 T MB spectra of 3FU cells (Figure 1A) were dominated by a sextet that collapsed into a doublet at 70 K (Figure 1B). This behavior and the apparent hyperfine splitting of the sextet (H_{eff} = 480 kG) and MB parameters for the resulting doublet (δ = 0.55 mm/s, and ΔE_Q = 0.25 mm/s) are typical of ferritin. We have assigned this feature as such (see Table 1 for a list of Fe-containing species found in these cells). Fe-bound ferritin represented approximately half of the Fe in the sample (52% of 220 μM = 114 μM). Assuming that this storage form of Fe is unnecessary for cellular metabolism, the remaining Fe concentration of ~100 μM in these cells matches the concentration of Fe in cells grown on unsupplemented medium. We suggest that Jurkat cells require ~100 μM cellular Fe for normal growth; this is the concentration of essential Fe in these cells.

The non-ferritin forms of Fe evident in the spectra of 3FU cells included the central doublet (CD) and non-heme high-spin (NHHS) Fe^{II} doublet. The CD primarily includes the S = 0 [Fe$_4$S$_4$]$^{2+}$ clusters and LS Fe^{II} hemes found in mitochondrial respiratory complexes. This doublet represented ~25% of the intensity (55 μM) of the 5 K low-field MB spectrum of Figure 1A. At 70 K, the ferritin sextet collapsed, revealing the high-energy line of a NHHS Fe^{II} doublet (simulated by the green line in Figure 1B). The NHHS Fe^{II} doublet represented 13% of the spectral intensity, which corresponds to ~30 μM Fe^{II} ions. The observed spectral parameters (δ = 1.3 mm/s, and ΔE_Q = 3.0 mm/s) are typical of Fe^{II} ions coordinated primarily by O and N ligands. These two species (the CD and NHHS Fe^{II}) represent the majority of the essential Fe in Jurkat cells.

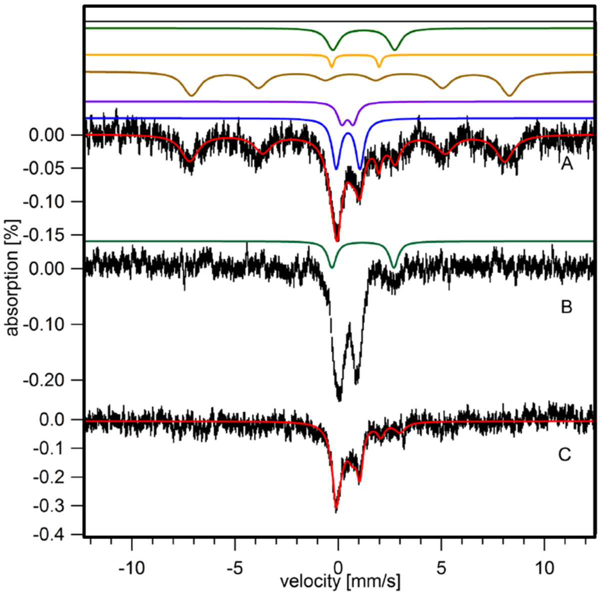

Figure 1. Mössbauer spectra of Jurkat cells grown in medium supplemented with 3 μM ^{57}Fe^{III} citrate: (A) 3 μM FC at 5 K and 0.05 T and (B) same as panel A but at 70 K. Simulations were as follows: CD (blue; δ = 0.46 mm/s, and ΔE_Q = 1.2 mm/s), Fe^{III} oxyhydroxide nanoparticles (purple; δ = 0.48 mm/s, and ΔE_Q = 0.57 mm/s), ferritin (brown; δ = 0.54 mm/s, ΔE_Q = 0.20 mm/s, and H_{eff} = 480 kG), HS Fe^{II} hemes (orange; δ = 1.0 mm/s, and ΔE_Q = 2.0 mm/s), and NHHS Fe^{II} (green; δ = 1.3 mm/s, and ΔE_Q = 3.0 mm/s). (C) The 5 K, 0.05 T MB spectrum of isolated mitochondria from cells grown with 3 μM FC. Total simulations for A and C are colored red.

Interestingly, Fe-deficient yeast cells that also contained only essential Fe exhibited significant contributions from the same two components.[26] Although the function of the NHHS Fe^{II} ions in yeast has not been established, most of it was not located in mitochondria.

The concentration of the ferritin protein complex in 3FU cells was determined by quantitative Western blotting (Figure 2 and Table 1) to be 0.3 μM, indicating an average of 400 Fe atoms per ferritin complex (114 μM Fe/0.3 μM ferritin). Populations of purified ferritin complexes afford binomial-like Fe loading distributions,[36,37] and we interpret our results similarly for *in vivo* ferritin populations.

We isolated mitochondria from 3FU cells. The Fe concentration of the organelle was low [280 μM (Table S1 of the Supporting Information)] compared to mitochondria isolated from 10FU cells.[28] Also, the corresponding 5 K low-field MB spectrum (Figure 1C) was weak. Nevertheless, the CD doublet clearly dominated the spectrum, corresponding to at least half of the total intensity. The degree of resolution between the two legs of the CD indicated that the level of Fe^{III} nanoparticles in the sample was low. HS Fe^{II} heme and NHHS Fe^{II} species contribute quadrupole doublets with well-defined δ and ΔE_Q values. Such doublets at ~5% intensity for each can be fit easily in the spectrum of Figure 1C (this is not conclusive evidence that such material is present, given the noise). Isolated mitochondria did not exhibit significant levels of a ferritin-like sextet. A minor ferritin-like feature could be distinguished from the baseline, but whether it arose from mitochondrial ferritin or a contaminant of cytosolic ferritin could not be determined (we suspect the latter).

The lack of a significant NHHS Fe^{II} doublet in the spectrum of isolated mitochondria indicates that the bulk of the

Table 1. Iron-Related Properties of Jurkat Cells[a]

sample	[FC] (μM)	[TBI] (μM)	k_r (h^{-1})	[Fe_{cell}] (*n*)	[ferritin protein], Fe/ferritin	Fe/S + LS hemes (%, μM)	HS Fe^{II} hemes (%, μM)	ferritin ([Fe_f]) (%, μM)	NHHS Fe^{II} ([Fe_c]) (%, μM)	nanoparticles ([Fe_n]) (%, μM)
0U, WT	0 + 6 = 6	0		100 ± 3 (*1*)	–, –	–	–	–	–	–
sim	4	0	0.8	105		31, 33 = [Fe_m]		64, 67	5, 5	0, 0
3FU, WT	3 + 6 = 9	0		220 ± 65 (*3*)	0.3, 380	25, 55	5, 11	52, 114	13, 29	5, 11
sim	9	0	1.0	216		38, 82		55, 119	13, 6	1, 2
10FU, WT	10 + 6 = 16	0		400 ± 70 (*5*)	0.3, 530	27, 108	4, 16	40, 160	11, 44	18, 72
sim	16	0	1.0	384		32, 124		38, 146	12, 45	18, 69
30FU, WT	30 + 6 = 36	0		840 ± 276 (*3*)	0.4, 275	13, 109	2, 17	13, 109	7, 60	65, 546
sim	36	0	1.0	865		16, 135		18, 157	10, 89	56, 483
100FU, WT	100 + 6 = 106	0		3700 ± 200 (*2*)	0.5, –	5, 185	–	–	–	93, 3440
sim	106	0	1.3	3307		4, 144		5, 167	5, 163	86, 2833
3TU, WT	0 + 6 = 6	3		142 ± 24 (*3*)	0.6, 95	40, 57	–, –	40, 57	–, –	–, –
sim	5	3	1.1	145		32, 46		63, 92	5, 7	0, 0
10TU, WT	0 + 6 = 6	10		160 ± 20 (*2*)	0.8, 80	40, 64	–	40, 64	–	–
sim	5	10	1.1	170		33, 56		61, 104	5, 9	0, 1
30TU, WT	0 + 6 = 6	30		225 ± 25 (*3*)	0.4, 300	30, 68	2, 5	54, 122	8, 18	6, 14
sim	5	30	1.1	209		37, 78		56, 117	6, 12	1, 2
3FL, WT	3 + 6 = 9	0		130 ± 6 (*2*)	0.4, 115	35, 46	2, 3	35, 46	11, 14	14, 18
sim	8	0	0.8	218		39, 86		56, 121	5, 10	0, 1
10FL, WT	10 + 6 = 16	0		580 ± 160 (*2*)	0.4, 290	26, 151	2, 12	20, 116	13, 75	38, 220
sim	16	0	1.1	598		23, 135		26, 157	10, 62	41, 244
30FL, WT	30 + 6 = 36	0		2000 ± 300 (*2*)	1.2, 167	10, 200	–, –	10, 200	–, –	79, 1580
sim	36	0	1.3	1591		9, 143		10, 165	7, 107	74, 1176
3TU, TfRC$^+$	0 + 6 = 6	3		400 ± 29 (*2*)	0.5, 480	25, 100	3, 12	60, 240	6, 24	2, 8
sim	6	3	1.2	302		38, 115		46, 138	10, 29	7, 20
10TU, TfRC$^+$	0 + 6 = 6	0		510 ± 14 (*2*)	0.7, 290	25, 127	2, 10	40, 204	3, 15	30, 153
sim	6	0	1.0	528		25, 130		29, 151	12, 63	35, 183
20FU, WT	20 + 6 = 26	0		675 ± 33 (*2*)	–	20, 135	2, 14	20, 135	4, 27	45, 304
sim	26	0	1.1	686		19, 133		22, 154	11, 77	47, 322
20FU (1:4), WT	0 + 6 = 6	0		225 ± 8 (*1*)	–	37, 83	2, 5	45, 90	10, 23	3, 7
sim	6	0	1.1	229		30, 69		45, 104	3, 8	21, 48
3TU (starved), WT	0 + 6 = 6	3		330 ± 5 (*1*)	–	19, 63	2, 7	50, 165	16, 53	13, 43
sim	5	3	2.6	328		36, 119		43, 141	11, 35	9, 31
10FU (Frxn$^-$)	10 + 6 = 16	0		550 ± 36 (*2*)	–	28, 154	3, 17	20, 110	5, 28	40, 220
sim	16	0	1.1	528		12, 64		27, 146	7, 37	53, 281

[a] WT indicates normal cells. TfRC$^+$ indicates cells overexpressing TfRC1. Frxn$^-$ indicates frataxin-deficient cells. Replicates *n* are given in parentheses where applicable. The concentration of endogenous Fe was assumed to be 4–6 μM and was added to the concentration of ferric citrate. For all simulations, $K_c = 9\ \mu M$, cs = 3, $K_m = 120\ \mu M$, $K_f = 130\ \mu M$, $k_t = 0.3\ h^{-1}$ (except for 3TU starved cells for which $k_t = 3\ h^{-1}$ and TfRC$^+$ cells for which $k_t = 1.8\ h^{-1}$), $k_m = 0.27\ h^{-1}$, $k_f = 0.55\ h^{-1}$, $k_{np} = 0.000045\ \mu M^{-1.9}\ h^{-1}$, and $p = 2.9$. Uncertainties are given in Table S3 of the Supporting Information. Values for k_r are given in the table. The unusually high value of k_r for 3TU starved cells suggests that the receptor for FC was also upregulated during the "starving" step of the experiment. $\alpha = 1/24\ h^{-1}$ for all simulations except for 10FL and 30FL, in which case $\alpha = 1/34\ h^{-1}$ and for Frxn$^-$ cells where $\alpha = 1/30\ h^{-1}$. For 20FU (1:4), the sample was diluted into medium without Fe supplementation and allowed to grow for two doublings. To simulate this, the initial Fe concentrations were set to those obtained for 20FU before dilution, and final Fe concentrations were recorded at 48 h. We illustrate how to read the table with the row beginning 3FU, WT and the next row labeled sim. The upper row includes the data, while the lower row includes the simulation. The overall concentration of FC in the experiment includes the 3 μM ^{57}Fe that was added to the medium plus 6 μM endogenous Fe. No TBI was added. The rate constant (k_r) used in the simulation was 1.0 h^{-1}. The cellular Fe concentration was 220 ± 65 μM (average of three experiments), while the simulation afforded a concentration of 216 μM. The concentration of ferritin protein in one of the samples was 0.3 μM, with an average loading of 380 Fe atoms per ferritin. The next five columns indicate the percentage of Fe in the sample due to particular groups of Fe centers (based on MB quantification). This is followed, after the comma, by the absolute concentration of that group (obtained by multiplying the percentage by [Fe_{cell}]/100). Simulated analogous values are given in bottom row of each pair. Two of the groups (Fe/S clusters + LS hemes combined with HS Fe^{II} hemes) were collectively considered "mitochondrial Fe_m" by the model. Thus, to compare the data and simulations for this category, one adds the two percentages in the data row (25% + 5% = 30%) and compares it to the percentage in the simulation row (38%). Likewise, one compares the sum of absolute concentrations (55 μM + 11 μM = 66 μM) in the data row to the value of 82 μM in the simulation row. In the four remaining columns, the experimental and simulated percentages and absolute concentrations can be compared directly. For Frxn$^-$ cells, the concentration of nanoparticles included both cytosolic (Fe_n) and mitochondrial (Fe_{mp}). Apart from the ferritin protein concentration, data given for 10FU were reported previously.[26]

associated NHHS Fe^{II} species observed in our whole cell spectrum was located in one or more nonmitochondrial regions

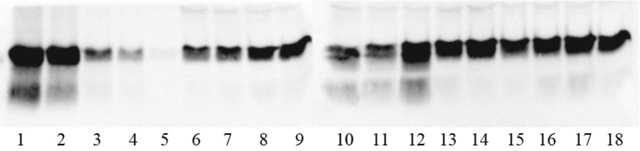

Figure 2. Quantitative Western blot of ferritin in cell lysates. The lanes were loaded with (1) 1000, (2) 500, (3) 100, (4) 50, and (5) 10 ng of holo-ferritin. The remaining lanes were loaded with 10 μL of lysates: (6) 3FU, (7) 10FU, (8) 30FU, (9) 100FU, (10) 3FL, (11) 10 FL, (12) 30FL, (13) 3TU, (14) 10TU, (15) 30TU, (16) 3TU TfRC$^+$, (17) 10TU TfRC$^+$, and (18) 30TU TfRC$^+$.

of the cell (assumed for this study to be the cytosol). This is similar to the Fe content of Fe-deficient yeast cells.[26] In a previous study,[28] we showed that the relationship

$$[\mathrm{Fe}]_{\mathrm{cell}} - [\mathrm{Fe}]_{\mathrm{ferritin}} = [\mathrm{Fe}]_{\mathrm{mito}} \frac{V_{\mathrm{mito}}}{V_{\mathrm{cell}}} + [\mathrm{Fe}]_{\mathrm{other}} \left(1 - \frac{V_{\mathrm{mito}}}{V_{\mathrm{cell}}}\right)$$

followed from the conservation of matter. We also found that $V_{\mathrm{mito}}/V_{\mathrm{cell}} \sim 0.2$ for Jurkat cells. Along with the concentrations obtained in this study for 3FU cells, this relationship and ratio suggest that ~50 μM Fe in these cells (primarily the NHHS Fe$^{\mathrm{II}}$ species) is found in regions other than mitochondria (e.g., the cytosol).

Equivalent samples of 3FU whole cells and their isolated mitochondria were characterized by EPR (Figures S3 and S4 of the Supporting Information) and UV−visible (Figure S5 and S6 of the Supporting Information) spectroscopies. EPR signals were weak, consistent with the low concentration of EPR-active Fe in these cells. Spectra included signals in the high-field and $g = 2$ regions. Observed resonances at $g = 6.3$ and 5.4 were assigned to the mixed-valence state (heme a_3 Fe$^{\mathrm{III}}$ Cu$_{\mathrm{b}}^{\mathrm{I}}$) of the cytochrome *c* oxidase active site.[28] The $g = 4.3$ signal was assigned to HS Fe$^{\mathrm{III}}$ species with rhombic symmetry. The $g = 2$ region included signals at $g = 2.00$, due to an unidentified organic radical, and g_{ave} values of 1.94 and 1.90, due primarily to mitochondrial respiratory complexes. The standard set of Fe$^{\mathrm{II}}$ heme UV−vis features was observed for all whole cell and isolated mitochondrial samples. Our analysis suggests that the Fe content of these mitochondria is similar to that reported previously.[28]

Fe Content of 30FU Cells. 30FU cells contained nearly 4 times more Fe than 3FU cells (Table 1) and 2 times more Fe than 10FU cells.[28] The corresponding 5 K low-field MB spectrum (Figure 3A) was dominated by a broad quadrupole doublet with parameters typical of Fe$^{\mathrm{III}}$ oxyhydroxide nanoparticles ($\delta = 0.48$ mm/s, and $\Delta E_{\mathrm{Q}} = 0.57$ mm/s). This doublet represented 65% of the Fe in the sample and corresponded to ~550 μM Fe (65% of the total Fe concentration of 840 μM). Nanoparticles were also present in 10FU cells, but their concentration was 7-fold lower.

The MB spectrum of 30FU cells also exhibited a ferritin-based sextet. Although barely distinguishable from baseline, the sextet represented ~13% of the Fe in the sample (0.13 × 840 μM = 109 μM). This concentration was almost the same as that of ferritin Fe in 3FU cells. Quantitative Western blotting (Figure 2) indicated ~0.4 μM ferritin protein in the sample, again suggesting partial Fe loading (109 μM/0.4 μM ≈ 300 Fe atoms/ferritin). A similar analysis of 10FU cells also indicated partial ferritin loading (160 μM/0.3 μM ≈ 500 Fe atoms/ferritin). The uncertainty in these determinations was such that loading ratios are considered to be essentially invariant for almost all conditions, with an average of 400 ± 100 Fe atoms/ferritin (3 and 10 μM TBI-grown cells have even lower loading ratios).

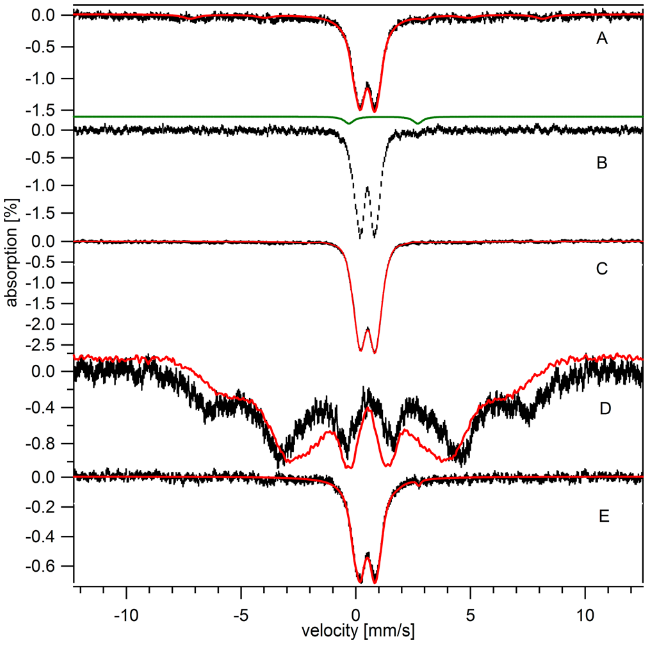

Figure 3. Mössbauer spectra of high-Fe Jurkat cells and mitochondria. (A), 30FU at 5 K and 0.05 T; (B), 30FU at 70 K and 0.05 T; (C), 100FU at 5 K and 0.05 T; (D), 100FU at 4.2 K and 6T (black) overlaid with a 6 T, 4.3 K spectrum (red) of yeast mitochondria isolated from Aft1-1$^{\mathrm{up}}$ cells.[62] (E) The 5 K, 0.05 T spectrum of mitochondria isolated from cells grown on glucose with 30 μM FC. Overall simulations for A and D are colored red.

The Fe associated with ferritin and nanoparticles collectively accounted for all but 185 μM Fe in the 30FU cells. Nanoparticles and ferritin-bound Fe probably do not contribute to cellular physiology; the majority of the remaining Fe is probably due to the essential Fe described above. The CD in the 5 K MB spectrum (Figure 3A) could not be cleanly resolved from the nanoparticle doublet; however, subtracting various percentages of a doublet fixed with CD parameters from the unresolved nanoparticle-dominated spectrum suggested that 10−15% of the spectral intensity (100−130 μM) was due to the CD. At 70 K, the ferritin sextet collapsed into a doublet revealing a NHHS Fe$^{\mathrm{II}}$ doublet (green line in Figure 3B) that corresponded to ~7% of the spectral intensity (60 μM Fe$^{\mathrm{II}}$). These two features, the CD and NHHS Fe$^{\mathrm{II}}$, undoubtedly represented much of the essential Fe in the sample. Somewhat lower concentrations of these two species were observed in the 3FU sample.

The extent of nanoparticle formation scaled nonlinearly with the concentration of Fe in the medium. 100FU cells were grown to maximize formation of these particles; such a sample was characterized by MB spectroscopy at 5 K and 0.05 T (Figure 3C). These cells accumulated 3.5−4 mM total Fe, >90% of which was in the form of nanoparticles. The corresponding 6 T spectrum (Figure 3D, black hashmarks) was dominated by a broad magnetic feature suggesting superparamagnetic behavior. This spectrum was compared to that of previously characterized Fe$^{\mathrm{III}}$ oxyhydroxide phosphorus-associated nanoparticles from the Aft1-1$^{\mathrm{up}}$ yeast strain[27] (Figure

3D, red line). Spectral features were similar but not identical, indicating a different distribution of hyperfine coupling constants. These magnetic differences must correspond, at some level, to structural differences.

MB spectra of mitochondria isolated from 30FU cells were also dominated by nanoparticles (Figure 3E and Table S1 of the Supporting Information). Approximately 690 μM Fe in these isolated organelles originated from nanoparticles, whereas the concentration of nanoparticles in corresponding whole cells was ~550 μM. Because mitochondria occupy ~20% of the cell's volume, we would expect that if all nanoparticles in the cell were present in these organelles, the concentration of nanoparticles in isolated mitochondria would be ~2.7 mM Fe (5 times more than observed). Furthermore, with increase in the FC concentration from 10 to 30 μM in the medium, the whole cell Fe concentration doubled, but the Fe concentration associated with isolated mitochondria did not change significantly. These considerations imply that the extra Fe in 30FU cells (primarily nanoparticles) accumulated in one or more nonmitochondrial regions, possibly in the cytosol.

Although the concentration of Fe in 30FU mitochondria was similar to that of 10FU mitochondria,[28] the MB distribution of that Fe was different. Mitochondria from the 30FU cells exhibited a significant decrease in the absolute concentration of ferritin-like Fe, HS Fe^{II} hemes, and NHHS Fe^{II}, as well as a significant increase in the concentration of nanoparticles (Table S2 of the Supporting Information). The diminished amount of ferritin-like Fe may be irrelevant given that ferritin is cytosolic. The difference in ferritin-like material is probably the consequence of small-number variations (we prepared two batches at each concentration) and less contamination in the 30FU samples. UV–vis analysis of these samples exhibited similar levels of cytochromes (Figure S6 of the Supporting Information). EPR spectra were also determined for 3FU and 30FU cells. The same group of signals, with similar intensities, was observed for these cells and the 10FU sample.[28] The spectral intensities of the CD component of MB spectra were similar for the samples. These characteristics, considered collectively, suggest that the concentrations of respiratory complexes in the mitochondria isolated from 3FU, 10FU, and 30FU cells were approximately the same. The major difference was the presence of more nanoparticles in the 30FU cells.

We were initially concerned that the doublet attributed to nanoparticles in these cells actually represented ferritin loaded with small amounts of Fe (≤10:1 Fe:ferritin ratio). At ~4 K, such species exhibit a quadrupole doublet rather than a sextet.[38] We reasoned that if the superparamagnetic doublet actually arose from poorly loaded ferritin, adding an excess of Fe^{II} under aerobic conditions would load the ferritin, causing the doublet to disappear and the sextet to appear. However, the results (Figure S2 of the Supporting Information) did not show such a shift, indicating that the majority of the broad doublet arose from nanoparticles rather than from poorly loaded ferritin.

EDX EM imaging of 30FU cells revealed ~1 nm diameter particles in what appears to be the cytosol (Figure 4C). Elemental mapping revealed that these particles were associated with both Fe and P in an approximately 1:1 molar ratio (Figure 4A,B and Figure S1 of the Supporting Information). Results for O were ambiguous because of strong background levels of O in the cytosol and/or in the embedding medium. Such nanoparticles were not detected by EDX imaging in 3FU or 3TU cells.

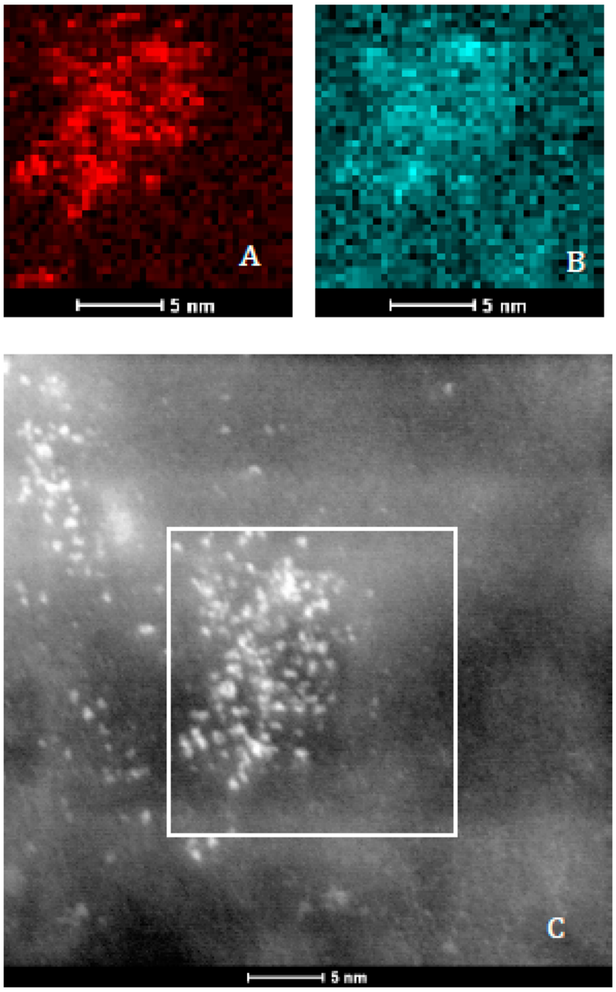

Figure 4. EDX images of glucose-grown cells in medium containing 30 μM FC: (A) Fe map, (B) P map, and (C) 320 K magnified image of Fe deposits. The box in panel C denotes the region in which the elemental maps were obtained.

Oxidative Damage.

In yeast cells, nanoparticle formation is reportedly associated with oxidative damage.[39,40] To investigate whether nanoparticle formation is associated with oxidative damage in human cells, we performed an Oxyblot analysis on 3FU 10FU, 30FU, and 100FU Jurkat cells (Figure 5, lanes 1–4). In this experiment, the level of oxidative damage increased modestly as FC and nanoparticle levels increased. In another experiment (Figure S7 of the Supporting Information),

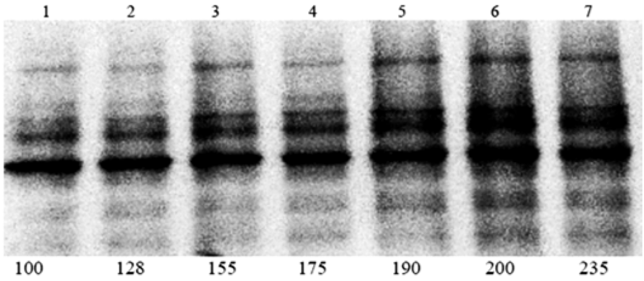

Figure 5. Oxyblot analysis of cells grown under different conditions. Samples included (1) 3FU, (2) 10FU, (3) 30FU, (4) 100FU, (5) 3FL, (6) 10FL, and (7) 30FL. Percentages of intensities relative to lane 1 are designated below each lane.

there was no correlation between ROS and Fe level. We conclude that there is little effect of nanoparticle formation on ROS levels in glucose-grown Jurkat cells.

Bioavailability of Nanoparticles. We wondered whether cells can utilize the Fe in nanoparticles. To examine this, cells were overloaded with nanoparticles (by growth in 20 μM ^{57}FC medium) and then transferred to unsupplemented medium. They were grown to their maximal density, and a portion was used to prepare a MB sample. The remaining cells were washed once with PBS containing 1 mM EGTA (to remove excess Fe), followed by another wash with PBS buffer lacking EGTA. The cells were diluted 4-fold in unsupplemented medium, allowed to grow to their maximal density (two doubling times), and then harvested. Significant amounts of nanoparticles accumulated in 20FU cells (Figure 6A), but nanoparticles were absent in the cells that were subsequently grown on unsupplemented medium; only the CD, ferritin, NHHS Fe^{II}, and HS Fe^{II} hemes were evident in the 5 K low-field MB spectrum (Figure 6B). Metal analysis combined with MB simulations of different Fe species (Table 1) indicated that the only feature that declined considerably in concentration (>40-fold decrease) upon growth of the split cells was nanoparticles. Other features remain roughly unchanged, with minor decreases attributed mainly to dilution due to growth of the cells. These results indicate that Jurkat cells can utilize nanoparticle Fe, converting it into mitochondrial Fe, ferritin, and presumably all other Fe-containing species required for cellular metabolism.

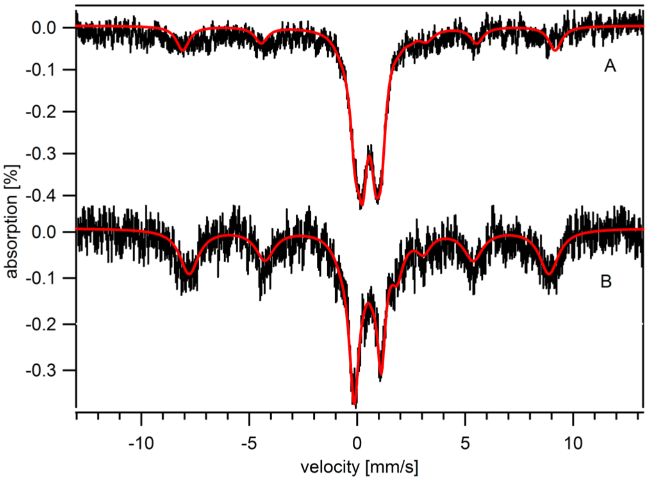

Figure 6. Bioavailability of nanoparticles: (A) 5 K, 0.05 T MB spectra of 20FU cells (half-filled cup) and (B) spectrum derived from panel A but after washing and further growth on medium unsupplemented with ^{57}Fe (filled cup).

Galactose-Grown Cells. Cells were grown with 3, 10, and 30 μM ^{57}FC in medium containing galactose rather than glucose as a carbon source. Approximately half as much Fe accumulated in 3FL cells as in 3FU cells. However, the Fe concentration of galactose-grown cells increased faster than that of glucose-grown cells as the FC concentration in the growth medium increased. The concentration of Fe in 10FL cells was ~50% higher than in corresponding glucose-grown cells. 30FL cells contained more than twice as much Fe as the corresponding glucose-grown cells (Table 1). Galactose-grown cells had a longer doubling time (~34 h), which may have promoted Fe uptake.

MB analysis revealed that 3FL cells were largely devoid of nanoparticles (Figure 7A and Table 1). Interestingly, the 5 K, 0.05 T MB spectrum of 10FL cells exhibited a 3-fold greater contribution from nanoparticles and a decline in the level of ferritin Fe relative to 10FU cells (Figure 7B and Table 1). The nanoparticle doublet obscured the CD in the MB spectrum of galactose-grown cells, but simulation of the MB spectrum afforded an estimate of the percentage of CD. A low-intensity NHHS Fe^{II} doublet was evident, with a concentration similar to that observed for 10FU cells. The absolute concentrations of nanoparticles (and possibly the CD) were significantly higher in 30FL cells than in equivalent glucose-grown cells (Figure 7C and Table 1). Distinguishing these two contributions is difficult because they are not well-resolved. UV−vis spectra of galactose-grown cells do not exhibit increased concentrations of cytochromes (Figure S5 of the Supporting Information), suggesting that there is no significant increase in the mitochondrial concentration (and thus no significant increase in the CD). The concentration of ferritin Fe also did not change considerably in galactose-grown cells as the FC concentration in the medium increased.

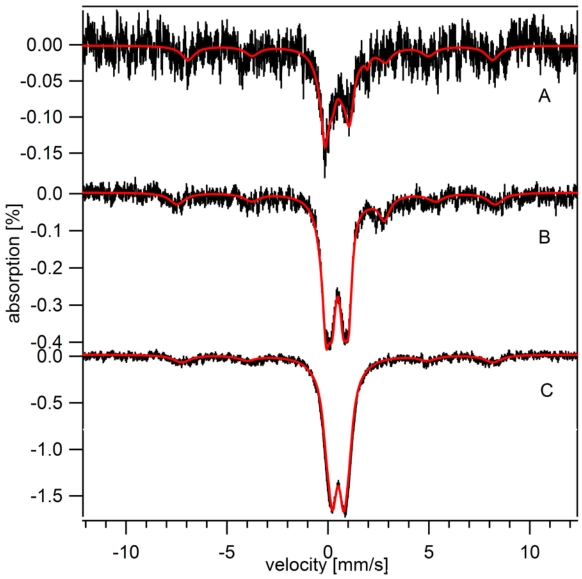

Figure 7. 5 K, 0.05 T Mössbauer spectra of galactose-grown cells: (A) 3FL, (B) 10FL, and (C) 30FL. Simulations are colored red.

The observed difference in nanoparticle level might be related to the different metabolic activity of galactose- versus glucose-grown cells, and/or to different growth rates. The oxygen consumption (OCR) rate of galactose-grown cells was 2−3 times greater than that of glucose-grown cells (Figure 8A). On the other hand, the extracellular acidification rate (ECAR) of the glucose-grown cells was 3−4 times greater than that of the galactose-grown cells. The OCR of cells grown under the two different carbon sources was also determined in the absence and presence of oligomycin (an inhibitor of F_1F_0 ATP synthase). The normalized OCR of glucose-grown cells decreased ~60% in the presence of oligomycin, whereas that of galactose-grown cells decreased almost ~80% (Figure 8B), indicating tighter coupling of respiration and ATP synthesis in galactose-grown cells.[35] These results confirm that our galactose-grown cells depended more heavily on oxidative phosphorylation (i.e., mitochondrial respiration) than on glycolysis for ATP production.

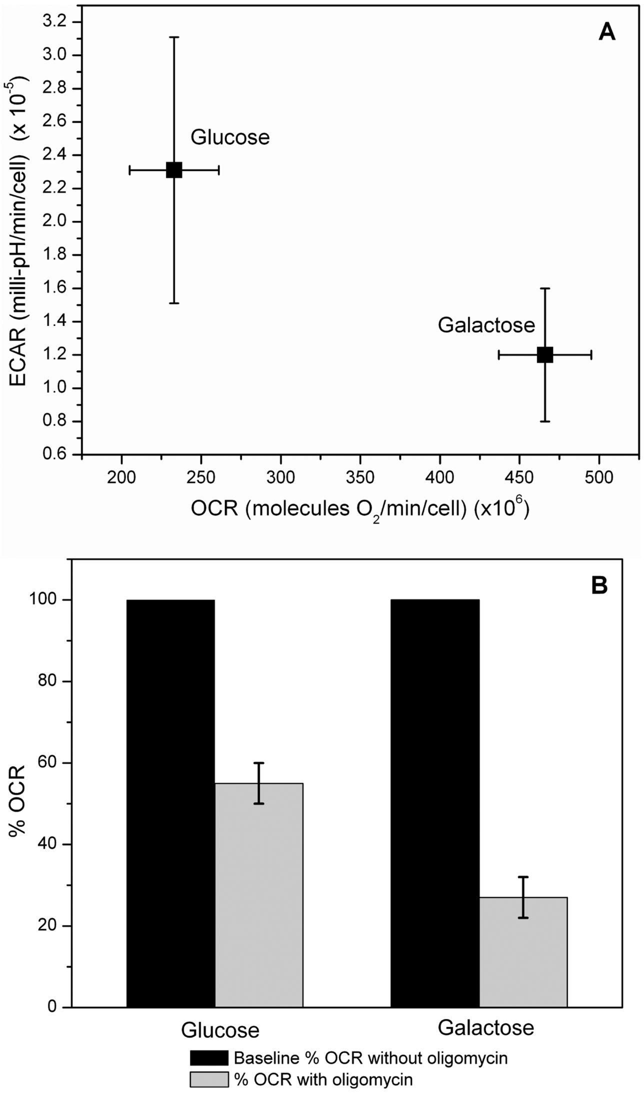

Figure 8. Oxygen consumption rate (OCR) and extracellular acidification rate (ECAR) of glucose- and galactose-grown cells. (A) Normalized ECAR vs OCR measurements of cells grown in glucose or galactose. (B) Normalized OCR measurements of cells grown in glucose or galactose in the absence (black) or presence (gray) of 1 μM oligomycin.

Oxidative Damage. Cells grown on galactose and FC exhibited ~50% higher levels of oxidative damage than cells grown on glucose and FC (Figure 5). The effect of cellular Fe concentration on the level of ROS damage was again minor, if there was any effect. The increased level of damage to galactose-grown cells may be caused by the greater dependency on mitochondrial respiration and oxidative phosphorylation for ATP production in galactose-grown cells.[41]

Increased Level of Transferrin Receptor Expression. Cells were grown on medium supplemented with 3TU. The total Fe concentration in such cells was quite low (~140 μM), and the level of ^{57}Fe enrichment was only ~50%. Consequently, the corresponding 5 K low-field MB spectrum (Figure 9A) had a low percent effect and was noisy. The general pattern indicated less ferritin and relatively more CD, compared to the Fe content of 3FU cells. Spectral noise precluded a more detailed analysis. MB spectra of mitochondria isolated from cells grown with 3TU (Figure 9C) exhibited little evidence of a nanoparticle doublet.

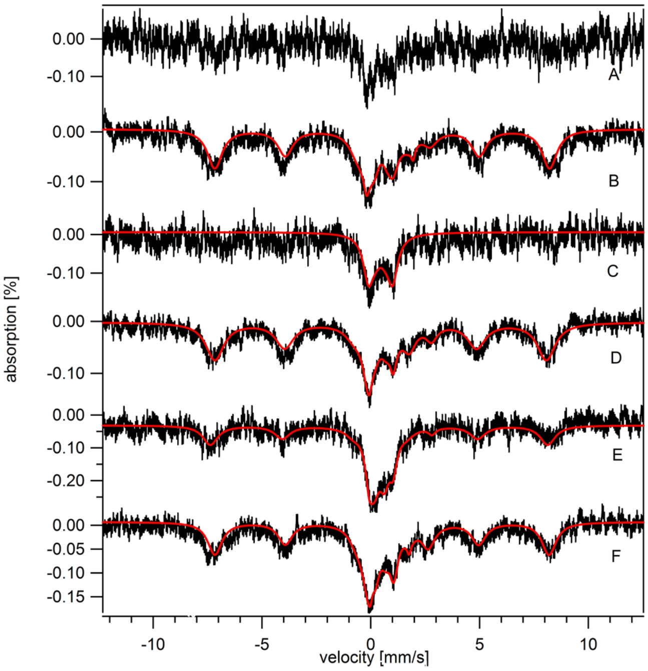

Figure 9. 5 K, 0.05 T Mössbauer spectra of Jurkat cells grown on TBI and mitochondria isolated therefrom: (A) 3TU WT, (B) 30TU WT, (C) mitochondria isolated from cells in part A, (D) 3TU TfRC$^+$, (E) 10TU TfRC$^+$, and (F) WT cells grown in unsupplemented glucose-containing medium with 100 μM DFO and then transferred to medium containing 3 μM ^{57}TBI. Red lines are overall simulations using percentages given in Table 1, and parameters given in the legend of Figure 1.

Increasing the ^{57}TBI concentration in the medium to 30 μM yielded an intracellular Fe concentration of 225 μM, which resulted in a more intense and analyzable 5 K low-field MB spectrum (Figure 9B). The spectrum was dominated by ferritin and CD Fe and displayed a negligible nanoparticle doublet (Table 1). The extent of ferritin loading was ~3 times larger than in 3TU or 10TU cells (Table 1) but was still low (~300 Fe atoms/ferritin) relative to full loading.

In an effort to increase the Fe concentration in TBI-grown cells, cells were genetically modified to overexpress ~3-fold more TfRC1 than normal (Figure S8 of the Supporting Information). Such cells (called TfRC$^+$) grown on 3 μM ^{57}TBI contained 3 times as much total Fe as equivalently grown WT cells. Correspondingly, the MB spectrum exhibited by the TfRC1$^+$ cells (Figure 9D) was more intense. Sixty percent of the Fe in the cells was ferritin-bound, which was the highest percentage of Fe found in this form for any cell condition examined. The sextet contribution was simulated and removed, revealing CD and NHHS Fe^{II} contributions. The spectrum included little if any nanoparticle doublet. TfRC$^+$ cells were also grown with 10 μM ^{57}TBI; such cells accumulated ~25% more Fe than cells grown with 3 μM ^{57}TBI. MB analysis of these cells revealed a more significant accumulation of nanoparticles (Figure 9E and Table 1).

We also attempted to stimulate WT cells to take up TBI by first starving them of Fe in the presence of DFO for 12 h (to upregulate TfRC1 expression) and then adding 3 μM ^{57}TBI to the growth culture. These cells incorporated ~3 times more ^{57}Fe than cells grown on 3 μM ^{57}TBI without this stimulation.

They accumulated Fe mainly in the form of ferritin and CD (Figure 9F and Table 1).

Reduced Level of Frataxin Expression. We also examined the Fe content of Jurkat cells in which the level of frataxin expression was reduced by RNAi. Western blot analysis indicated that the expression level of frataxin in frataxin-deficient cells was 30−50% of that of WT levels in cells grown under the same conditions (10 μM FC) (Figure S9 of the Supporting Information). Significantly more nanoparticles accumulated in frataxin-deficient cells grown with 10 μM FC than in 10FU cells (Figure 10 and Table 1). The concentration of nanoparticles detected by MB spectroscopy was ~3 times greater in frataxin-deficient cells (220 μM) than in WT cells (72 μM). More total cellular Fe accumulated in these cells (550 μM) than in WT cells (400 μM), with most of the excess Fe present as nanoparticles. UV−vis analysis indicated an ~40% decline in cytochrome levels of frataxin-deficient cells relative to that of WT cells (Figure S10 of the Supporting Information).

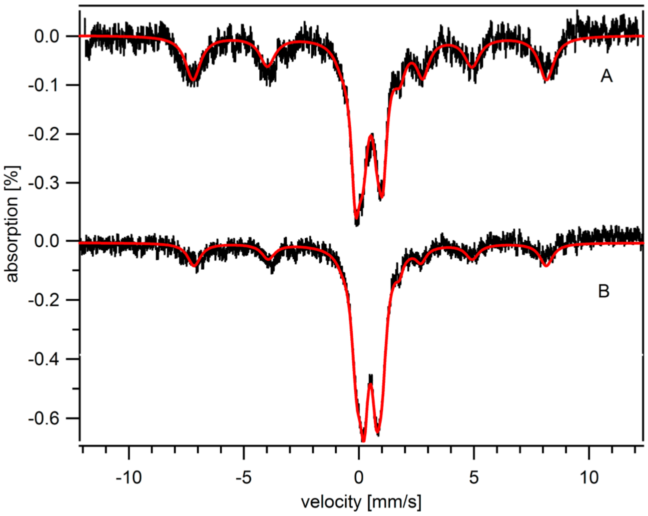

Figure 10. Effect of frataxin deficiency: (A) 5 K, 0.05 T MB spectrum of WT 10FU and (B) spectrum of frataxin-deficient cells grown with 10 μM FC. Total simulations are colored red using percentages listed in Table 1.

■ ANALYSIS

We analyzed our data by developing a chemical model for the Fe import and trafficking pathways in Jurkat cells (Figure 11). Cellular Fe was assumed to be composed of four species, namely, $[\mathrm{Fe_{cell}}] = [\mathrm{Fe_c}] + [\mathrm{Fe_f}] + [\mathrm{Fe_m}] + [\mathrm{Fe_n}]$. Fe could enter the cell by either TBI or FC import pathways. Both pathways merged at $\mathrm{Fe_c}$, an unidentified cytosolic Fe species presumed to correspond to the NHHS $\mathrm{Fe^{II}}$ spectral feature observed in MB spectra of Jurkat cells. According to the model, $\mathrm{Fe_c}$ can react to form $\mathrm{Fe_f}$, $\mathrm{Fe_m}$, and $\mathrm{Fe_n}$, which represent the Fe associated with ferritin, mitochondria, and nanoparticles, respectively. $\mathrm{Fe_m}$ is the sum of cellular Fe−S clusters and hemes, which we assumed to be originating exclusively from mitochondria.

The model of Figure 11 was translated into ordinary differential equations (ODEs) (eqs 1−4) that describe the factors influencing the changes in concentration of each cellular component.

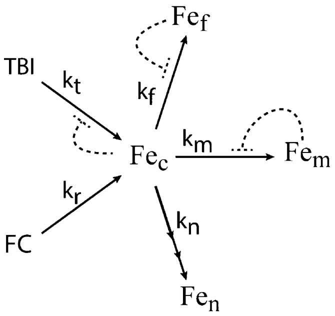

Figure 11. Model of Fe import and intracellular trafficking in Jurkat cells. Solid arrows indicate reactions associated with rate constants k_t, k_r, k_f, k_m, and k_n. Reactions k_t and k_r represent import of TBI and FC Fe, respectively. Reactions k_f and k_m represent transfer of $\mathrm{Fe_c}$ to ferritin and mitochondria, respectively. Reaction k_n represents conversion of cytosolic Fe into nanoparticles. Dashed lines terminating at short straight orthogonal segments represent regulation sites. The lines emanate from the sensed form of Fe. The triple-headed arrow indicates a higher-order dependence of $\mathrm{Fe_c}$ on that reaction.

$$\frac{d[\mathrm{Fe_c}]}{dt} = \frac{k_t[\mathrm{TBI}]}{1 + \left(\frac{[\mathrm{Fe_c}]}{K_c}\right)^{\mathrm{cs}}} + k_r[\mathrm{FC}] - \frac{k_m[\mathrm{Fe_c}]}{1 + \left(\frac{[\mathrm{Fe_m}]}{K_m}\right)^{\mathrm{ms}}} - \frac{k_f[\mathrm{Fe_c}]}{1 + \left(\frac{[\mathrm{Fe_f}]}{K_f}\right)^{\mathrm{fs}}} - k_n[\mathrm{Fe_c}]^p - \alpha[\mathrm{Fe_c}] \qquad (1)$$

$$\frac{d[\mathrm{Fe_f}]}{dt} = \frac{k_f[\mathrm{Fe_c}]}{1 + \left(\frac{[\mathrm{Fe_f}]}{K_f}\right)^{\mathrm{fs}}} - \alpha[\mathrm{Fe_f}] \qquad (2)$$

$$\frac{d[\mathrm{Fe_m}]}{dt} = \frac{k_m[\mathrm{Fe_c}]}{1 + \left(\frac{[\mathrm{Fe_m}]}{K_m}\right)^{\mathrm{ms}}} - \alpha[\mathrm{Fe_m}] \qquad (3)$$

$$\frac{d[\mathrm{Fe_n}]}{dt} = k_n[\mathrm{Fe_c}]^p - \alpha[\mathrm{Fe_n}] \qquad (4)$$

The first term on the right-hand-side of eq 1 describes the rate of import of TBI through the TfRC1 on the plasma membrane. Regulation of this and two other rates in the model are described by the function

$$\mathrm{Reg\_}(\mathrm{Fe_s}, K_s, s) = \frac{1}{1 + \left(\frac{[\mathrm{Fe_s}]}{K_s}\right)^{s}}$$

in which species $\mathrm{Fe_s}$ is sensed by the regulatory system, K_s is an apparent inhibition constant associated with the sensing event (also called a set-point concentration), and s is a sensitivity parameter. Reg_ is a form of the Hill equation that we have used as a surrogate for poorly defined or highly complex regulatory mechanisms. Reg_ could reflect the direct (or indirect) binding of $\mathrm{Fe_s}$ to (a) the promoter of a gene (i.e., transcriptional regulation), (b) an mRNA strand (translational regulation), or (c) an allosteric site of a protein (enzyme regulation). Reg_ can be viewed as a valve that opens wide when $[\mathrm{Fe_s}] < K_s$, shuts when $[\mathrm{Fe_s}] > K_s$, and is half-open when $[\mathrm{Fe_s}] = K_s$. The rate of TBI influx is regulated by Reg_, with $\mathrm{Fe_c}$ serving as $\mathrm{Fe_s}$. In this case, Reg_ is a surrogate for the Fe-dependent binding of IRP1 and IRP2 to the mRNA of the transferrin receptor mRNA.

The second term of eq 1 reflects the unregulated import of FC. Our model is minimal in that no unnecessary terms are included. We could fit the data in Table 1 acceptably well without assuming that the import of FC was regulated. The third term of eq 1 reflects the flow of Fe_c into mitochondria. The rate of mitochondrial Fe import via mitoferrin1 and -2 is regulated, but the mechanism has not been established in nonerythroid cells, except for the fact that these proteins are regulated post-translationally.[42,43] The sensed molecule in this process was assumed to be the concentration of Fe_m.

The fourth term of eq 1 reflects the loading of Fe into ferritin. IRP1 and IRP2 also regulate ferritin synthesis in an Fe-dependent manner, stimulating production of ferritin under high-Fe conditions.[6] We initially tried to regulate the system in this manner [by multiplying the rate of Fe loading into ferritin (k_f) by the function $Reg_+ = 1 - Reg_-$, using Fe_c as the sensed molecule], but the resulting behavior was not satisfactory, as the observed ferritin concentrations changed significantly less than the simulated concentrations. This suggested that the regulation of ferritin loading was more like the regulation of mitochondrial Fe import. Thus, we employed the Reg_- function in the manner used to regulate mitochondrial Fe import, assuming that the sensed Fe_s was ferritin Fe_f.

The fifth term of eq 1 refers to the rate of nanoparticle formation. We initially assumed a first-order dependence of the Fe_c concentration in this process, but our simulations could not reproduce the disproportionate increase in the concentration of nanoparticles (Fe_n) that occurred when the FC concentration in the growth medium increased (e.g., from 3 to 30 μM or from 3 to 100 μM). Mimicking this behavior required that we assumed a higher-order dependence on Fe_c concentration (Table 1). This order dependence is consistent with a mechanism in which multiple (approximately three) Fe ions react at or before the rate-determining step in the formation of nanoparticles.

The last term of eq 1 reflects dilution due to cell growth. In our model, the cell is growing as Fe is imported, such that a steady-state Fe_{cell} concentration is eventually achieved (the Fe concentration data of Table 1 were interpreted as representing steady-state values). Each component of a growing cell requires a dilution term in its ODE.[44] The growth rate α was assumed to be the inverse of the doubling time.

The sum of ODEs 1−4

$$\frac{d[Fe_{cell}]}{dt} = \frac{k_t[TBI]}{1 + \left(\frac{[Fe_c]}{K_c}\right)^{cs}} + k_r[FC] - \alpha[Fe_{cell}]$$

defines how the overall Fe concentration of the cell changes over time. In the absence of TBI and under Fe-limiting steady-state growth conditions, $k_r[FC] = \alpha[Fe_{cell}]$. [FC] in this equation includes not only the concentration of ferric citrate in the medium but also the concentration of endogenous Fe (4−6 μM). In the absence of additional added FC, $[Fe_{cell}] \approx 100$ μM and [FC] = 4 μM, such that a DT of 24 h implies that $k_r \approx 0.7$ h^{-1}. When cells are grown on 100 μM FC, $[Fe_{cell}] = 3500$ μM, [FC] = 106 μM, and thus $k_r \approx 1.3$ h^{-1}. We view this range for k_r (1.0 ± 0.3) as acceptable, given the simplicity of the model.

Sensitivity factors ms and fs were set semiarbitrarily to 10 to provide extremely tight regulation. The other parameters of the system (cs, K_c, K_m, K_f, k_t, k_m, k_f, k_n, and p) were estimated by attempting to simulate the entire data set of Table 1. The ODEs were numerically integrated using Maple (http://www.maplesoft.com/). Growth conditions of the simulation model cell were varied to mimic the conditions listed in Table 1. For $TfRC^+$ cells, the constitutive overexpression of TfRC was mimicked by assuming a 6-fold faster import rate constant k_t and by removing the Reg_- term. Cells grew slower on galactose than on glucose (DT = 34 h rather than 24 h), so α was adjusted accordingly for those simulations. Each simulation was allowed to continue for 1000 h (where time refers to that indicated in the ODEs) to ensure that steady-state conditions had been achieved. Resulting simulated concentrations are listed in Table 1. The uncertainties associated with the data were estimated to be ±20%, so that discrepancies between simulations and data within this range are considered irrelevant. The model is simple, semiquantitative, and foundational. It captures the essential features of Fe import and trafficking in Jurkat cells but lacks many details associated with these processes.

One advantage of ODE models is that they have predictive power. Thus, our model can predict the distribution of these four forms of Fe in Jurkat cells grown with any concentration of TBI or FC. It can also be modified to explore genetic changes in the cell, such as the consequences of reducing the level of expression of frataxin. Previous studies in yeast and mice have shown that a frataxin deficiency causes the accumulation of nanoparticles in mitochondria. This leads to an Fe deficiency condition in the cytosol.[30,45,46] To examine how our model would respond to this phenotype, we allowed for the possible formation of nanoparticles in the mitochondria by adding the term $-k_{np}[Fe_m]^p$ to ODE 3 and by adding ODE 5

$$\frac{d[Fe_{mp}]}{dt} = k_{mp}[Fe_m]^{mp} - \alpha[Fe_{mp}] \tag{5}$$

to the set of ODEs 1−4. For simplicity, we assumed that the kinetics of nanoparticle formation in the mitochondria were the same as those for nanoparticle formation in the original model (presumably in the cytosol). As such, we assigned the same values to k_{mp} and mp that were assigned to k_{np} and p, respectively.

As a control, we solved the new system assuming $k_{mp} = 0$ and $\alpha = 1/24$ h^{-1} so as to mimic WT expression levels of frataxin and the growth rate of WT cells. Resulting steady-state simulated concentrations are shown in the early region of the plot of Figure 12. We then set k_{mp} to 0.00045 h^{-1} and α to 1/30 h^{-1} to stimulate mitochondrial nanoparticle formation and mimic the slower-growing frataxin-deficient cells. The overall Fe concentration increased in our simulations from 461 to 528 μM, similar to the final state observed experimentally. The predicted time dependences of these changes should be evaluated experimentally, but this is beyond the scope of this study. The simulated response included an increase in the number of mitochondrial nanoparticles as well as a decline in the level of non-nanoparticle forms of mitochondrial Fe (interpreted as Fe−S clusters, hemes, and the pool of NHHS Fe^{II}). These changes are consistent with the deficiencies of Fe−S clusters and hemes that are associated (along with the dominance of nanoparticles) with the frataxin phenotype.[47] The simulated response to frataxin deficiency also included a decline in the level of cytosolic and ferritin Fe, consistent with the cytosolic Fe deficiency phenotype that has been reported.[46] We repeated the simulation at an FC concentration of 3 μM, but no phenotype was evident.

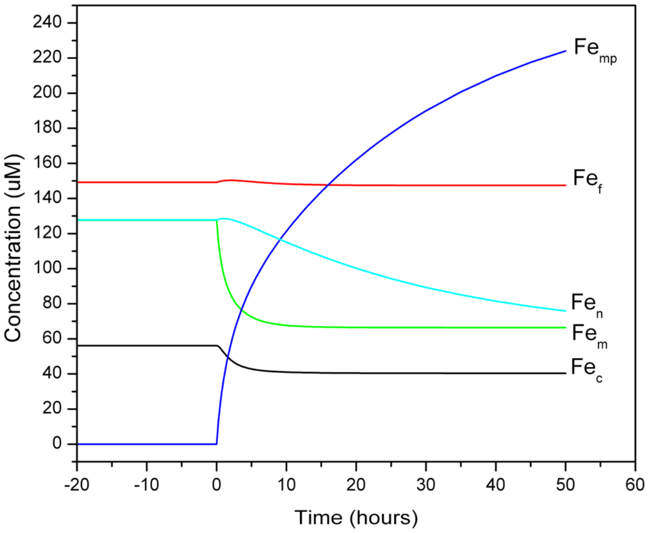

Figure 12. Simulation of the changes in the cellular iron distribution following frataxin depletion. The simulation at $t < 0$ is of WT glucose-grown cells in 10 μM FC, with DT = 24 h and $k_{mp} = 0$. At $t = 0$, k_{mp} was set to 0.000045 h^{-1} and DT to 30 h.

DISCUSSION

Using MB spectroscopy and other biophysical methods, we have investigated the Fe import pathways and downstream trafficking of two forms of Fe in human Jurkat cells, namely, transferrin-bound iron (TBI) and ferric citrate (FC). We did this by characterizing the Fe content of such cells grown in media containing different concentrations of TBI and/or FC and different carbon sources (glucose vs galactose). We also investigated cells in which the expression levels of the transferrin receptor and frataxin were altered. We developed a mathematical model of Fe import and trafficking in these cells and fit simulations obtained therefrom to our data.

TBI and FC Import Pathways. Our data and simulations indicate that the import of TBI iron is highly regulated. Our model suggests that cytosolic Fe regulates TBI import in accordance with a set-point concentration of ∼9 μM. In contrast, the import of FC does not appear to be regulated, or at least our model did not require that assumption. Whether the same holds true for other forms of NTBI remains to be determined, but we regard this as a viable possibility.

The fate of TBI (after DMT1-mediated export from endosomes into the cytosol) and the fate of FC within the cell are largely unknown. An earlier version of the model assumed two forms of cytosolic Fe, one derived from TBI and the other from FC. However, this assumption did not improve the fits, so we merged the two import pathways immediately once Fe entered the cytosol. In real cells, the pathways may not merge immediately. However, they must eventually merge. Fe from either source eventually moves into mitochondria (via the IM transporters mitoferrin1 and -2[48]), loads into ferritin (via PCBP1 and -2 chaperones[49,50]), and forms nanoparticles. There is probably no dedicated protein chaperone that transports Fe into nanoparticles. Rather, these particles appear to form spontaneously via chemistry of which the cell is unaware.

The distribution of Fe in TBI-grown cells differs relative to that in cells grown at the same FC concentration, primarily because less Fe overall is imported into TBI-grown cells. This is due, in turn, to the tighter regulation of TBI import. The higher concentration of cytosolic Fe in FC-grown cells increases the rate of nanoparticle formation disproportionately, such that it dominates the Fe content of FC-grown cells but not that of TBI-grown cells. Consistent with this, TBI-grown cells in which the transferrin receptor was constitutively overexpressed contained higher concentrations of Fe than WT cells grown on TBI. The distribution of Fe in these cells was similar but not identical to that observed in FC-grown cells.

Another likely reason for the different Fe distributions is that the TBI pathway may somehow favor storing Fe as ferritin relative to the FC pathway, which tends to funnel more Fe into nanoparticles. Our current model does not include such distinctions, but the possibility of distinct intracellular pathways should be considered when developing more advanced models. Supporting such a distinction at the protein expression level, our data show a more sensitive upregulation of ferritin protein in TBI-grown cells than in FC-grown cells. For example, 3TU cells had twice the concentration of ferritin compared to that of 3FU cells. This suggests that the system of IRP1 and IRP2 of regulation responds more sensitively to Fe_c derived from TBI. Furthermore, the same cellular Fe concentration accumulated in $TfRC^+$ cells grown on 3 μM TBI as in 10FU WT cells, but that Fe included significantly fewer nanoparticles and more ferritin Fe. Our simple model cannot account for such differences.

Mitochondria. The concentrations of mitochondrial Fe centers, including Fe−S clusters, hemes, and HS Fe^{III} ions, do not change drastically with an increase in the medium Fe concentration. This indicates the ability of mitochondria to regulate their own Fe import. The expression of the only known Fe transporters in the mitochondrial membrane, mitoferrin 1 and mitoferrin 2 (Mfrn1 and Mfrn2, respectively), is tightly regulated to prevent excessive mitochondrial Fe accumulation.[43] To mimic this invariance, our model tightly regulated mitochondrial Fe import using mitochondrial Fe itself as the sensed species. Clearly, not all mitochondrial Fe is sensed. Nevertheless, this regulatory assumption would remain viable as long as the concentration of the sensed molecule was proportional to the overall mitochondrial Fe concentration. The concentration of nanoparticles in mitochondria does seem to increase with the concentration of Fe in the medium. Again, this form of Fe may not be regulated by the cell; indeed, the cell may be unaware of its existence.

Ferritin. The extent of loading of Fe into ferritin was 1 order-of-magnitude lower than the often-quoted value of 4500 Fe atoms per core. Moreover, the extent of loading did not increase with increasing Fe concentration in the growth medium (which we presume is proportional to the cytosolic Fe concentration). Both results were surprising.

The low average extent of loading is undoubtedly due to a distribution of loading levels in a population of ferritin molecules. Ferritin loading distributions have been previously described for ferritin purified from various organs, using ultracentrifugation[51] or MB spectroscopy coupled with electron microscopy.[36,52] Bovell et al. obtained similar results by performing *in situ* electron microscopy coupled with ASAX analysis on rat liver sections.[37] We suggest a binomial distribution of Fe loadings in ferritin populations of Jurkat cells, with a maximum approaching 4500 Fe atoms/ferritin and a mean near ∼400 Fe atoms/ferritin. Our studies also suggest that the average ferritin load remains approximately the same regardless of the overall Fe concentration in the cell (though perhaps lower loads in 3TU and 10TU cells). Our results are consistent with an EM study showing a distribution of ferritin loading in iron-overloaded rat livers.[37]

The popular explanation of IRP1 and IRP2 regulation of ferritin is that the unbinding of these proteins from the ferritin message under high cytosolic Fe concentrations promotes ferritin synthesis so that excess cytosolic Fe can be removed from the cytosol and stored in ferritin.[6] The implication is that without this promotion, there would be no way for excess cytosolic Fe to be removed, because the existing ferritin was already fully loaded. The regulation of ferritin and the extent of loading do not appear to be so simple, at least in Jurkat cells. Cells containing partially loaded ferritin responded to increasing (cytosolic/medium) Fe concentrations by synthesizing more ferritin proteins, not by loading preexisting ferritin to the fullest possible extent. Another spurious initial notion of ours was that nanoparticles would form only once the cell exhausted its ferritin binding capacity. In contrast, we found that the ferritin was partially loaded in FC-grown cells that also contained substantial quantities of nanoparticles.

One explanation of this partial loading behavior is that the set-point concentrations for ferritin synthesis and Fe loading of ferritin differ. The set-point concentration of the Fe species that regulates the synthesis of new ferritin protein (via the IRP1 and IRP2 system) might be lower than the concentration of Fe required to fully load ferritin. In this way, as cytosolic Fe levels increase, they trigger further ferritin protein synthesis such that existing ferritin never becomes fully loaded.

Another shift in our thinking arose from our attempt to model the concentration of ferritin Fe in cells grown under different conditions. The concentration of ferritin Fe was roughly invariant among all of the conditions tested and examined by MB spectroscopy (Fe-limited cells and Fe-overloaded cells could not be investigated by MB). We initially attempted to model this using the well-known IRP1 and IRP2 mechanism. This required a Reg_+ function in which $\mathrm{Fe_c}$ was sensed. However, this resulted in greater variation in Fe ferritin levels than was evident in the data. Thus, we abandoned that form of regulation and employed a Reg_- function in which ferritin $\mathrm{Fe_f}$ was sensed (we did this after noting how well mitochondrial Fe could be regulated by assuming the Reg_- function with $\mathrm{Fe_m}$ as the sensed molecule). This arrangement adequately reproduced ferritin Fe levels under the various circumstances examined. However, the molecular-level mechanism responsible for this form of regulation is not understood; it seems unlikely that ferritin Fe could directly be sensed because it is an aggregated form. The rate of import of Fe into ferritin might be inhibited as the degree of ferritin loading reaches some critical threshold, as has been suggested on the basis of the rates of ferritin loading *in vitro*.[53,54]

Nanoparticles. The nanoparticles that accumulate in Jurkat cells are similar in chemical composition to those found in strains of yeast that have mutations in Fe−S cluster metabolism proteins.[39,40] The differences in high-field MB spectra, relative to yeast nanoparticles, suggest modest structural differences. Previous MB studies of the spleens of β-thalassemia patients[55] indicate accumulation of a species with MB parameters similar to those of the nanoparticle doublet observed here. Ferric phosphate nanoparticles accumulate in the hearts of mice displaying symptoms of Friedreich's ataxia.[29] The size of the particles observed in our cells (~1 nm) is substantially smaller than the size of ferritin particles (2.8−8 nm),[36,56] and they contain more phosphorus than ferritins.[57] Our results suggest that the majority of nanoparticles formed in these cells are nonmitochondrial. Our EM results suggest that nanoparticles form in the cytosol, and this was assumed by our model.

Our model suggests that the rate of nanoparticle formation is not regulated. This is consistent with the idea that the cell is unaware that nanoparticles are forming, suggesting that this is a purely chemical phenomenon. Although nanoparticles cannot be sensed by the cell, they may nevertheless play a role in cellular metabolism. We found that nanoparticle formation is reversible and that nanoparticle Fe can be recycled by the cell.

Our model required that the rate of nanoparticle formation depend on the cytosolic Fe concentration to higher than first order. This high-order rate dependence leads to the observed "burst" phenomenon in which there is a disproportionate increase in the concentration of nanoparticles as the $\mathrm{Fe_c}$ concentration increases. It implies that more than one $\mathrm{Fe^{III}}$ ion (nominally three such ions, according to our simulations) come together to form nanoparticles at or before the rate-determining step in the process.

Oxidative Damage. The lack of correlation between the extent of nanoparticle formation and oxidative damage in FC-grown cells grown on glucose is consistent with the results of Hartwig et al., who found that oxidative damage to DNA and lipid peroxidation in glucose-grown mammalian cells is not induced by growth on up to 2 mM FC.[58,59] $\mathrm{Fe^{III}}$ nanoparticles form from the oxidation of $\mathrm{Fe^{II}}$ ions, but whether this generates ROS (or is promoted by ROS) is uncertain. Our results indicate that the overall level of cellular ROS damage does not correlate significantly with cellular Fe or nanoparticle levels. Nanoparticle formation may generate (or be generated by) small amounts of ROS, but this does not impact cellular ROS levels significantly.

ROS can be scavenged by catalases, peroxidases, and antioxidants.[60,61] Perhaps the observed extent of oxidative damage is inversely related to the rate of these repairs. Also, the metabolic mode and growth rate may be factors in the level of cellular ROS damage. These considerations are supported by our finding that galactose-grown cells (which are more active in terms of respiration and also grow more slowly) are associated with greater ROS damage.

Our results and conclusions regarding the insignificance of nanoparticle formation on overall cellular oxidative damage are literally opposite of that proposed by Whitnall et al.,[29] who identified nanoparticles in the hearts of frataxin-deficient mice. They proposed that nanoparticles may be an "explosive" (their emphasis) source of ROS in such diseased heart tissue. Our data suggest that nanoparticle formation has little impact on cellular ROS levels.

Frataxin. Although simple, our model reproduces the major effects of depleting cells of frataxin. Besides nanoparticles accumulating in the mitochondria (which was designed into the model), other cellular Fe species in the model responded in ways that are also observed experimentally. Frataxin-deficient cells "feel" Fe-deficient in the cytosol, because of the increased rate of import of Fe into mitochondria. This effect was re-created in our simulations. Importantly, there was no alteration of the regulation of the entire system, including the regulation of import of Fe into the mitochondria themselves. The increase in total mitochondrial Fe (including $[\mathrm{Fe_m}]$ + $[\mathrm{Fe_{mp}}]$) was associated with the decline in $[\mathrm{Fe_m}]$ as this form of Fe was used to make mitochondrial nanoparticles. This decline stimulated further import of Fe into the organelle, which created a deficiency of Fe in the cytosol. Importantly, this imbalance of Fe in the cell was due to the formation of nanoparticles in the mitochondria, not to malfunctioning regulatory systems. Our study and model suggest that there is nothing "wrong" with Fe regulation in cells that are deficient in frataxin (or by extension, in patients with Friedreich's ataxia). The problem is that a deficiency of frataxin somehow alters the mitochondrial matrix so that it favors nanoparticle formation. This might involve changes in pH, redox state, or chemical composition. Understanding the mechanistic basis of these alterations will be critical in understanding and treating the disease.

Mathematical Modeling. Interpreting changes in cellular Fe metabolism (or any other complex cellular metabolic subsystem) on the molecular and mechanistic level is difficult, as the complexity of these systems is enormous. As more molecular-level interactions are discovered and characterized, it becomes increasingly difficult (and will eventually become impossible) to draw mechanistic inferences based merely on mentally contemplating such interactions. Gaining mechanistic insights will increasingly require the aid of mathematical models that can include an unlimited number of relationships explicitly and can integrate their collective effects.

■ ASSOCIATED CONTENT

Ⓢ Supporting Information

Analytical properties of isolated mitochondria (Table S1), concentrations of reduced hemes *a*, *b*, and *c* in Jurkat cells and isolated mitochondria (Table S2), TEM image of a Jurkat cell (Figure S1), a test to distinguish weakly loaded ferritin from nanoparticles (Figure S2), X-band EPR spectra of Jurkat cells (Figure S3), EPR spectra of isolated mitochondria (Figure S4), UV−vis spectra of whole Jurkat cells (Figure S5), UV−vis spectra of isolated mitochondria (Figure S6), Oxyblot analysis of cells grown under different conditions (Figure S7), Western blot indicating overexpression of TfRC (Figure S8), Western blot indicating knockdown of frataxin (Figure S9), UV−vis spectra of frataxin-deficient cells versus normal cells (Figure S10), and uncertainties in model parameters (Table S3). This material is available free of charge via the Internet at http://pubs.acs.org.

■ AUTHOR INFORMATION

Corresponding Author

*E-mail: lindahl@chem.tamu.edu. Phone: (979) 845-0956. Fax: (979) 845-4719.

Funding

This study was funded by the National Institutes of Health (GM084266), the Robert A. Welch Foundation (A1170), and the National Science Foundation (DMS-0714896).

Notes

The authors declare no competing financial interest.

■ ACKNOWLEDGMENTS

We thank Ann Ellis and Hansoo Kim at the Microscopy and Imaging Center at Texas A&M University for help in collecting images.

■ ABBREVIATIONS

BPS, bathophenanthroline sulfonate; CD, central quadrupole doublet; DFO, desferrioxamine; DDDI, double-distilled and deionized; DMT1, divalent metal transporter 1; δ, isomer shift; ΔE_Q, quadruple splitting; DT, doubling time; ECAR, extracellular acidification rate; EDTA, ethylenediaminetetraacetic acid; EDX, energy-dispersive X-ray; EM, electron microscopy; EPR, electron paramagnetic resonance; FC, ferric citrate; Fe_{cell}, overall cellular Fe; Fe_c, cytosolic Fe; Fe_f, ferritin-bound Fe; Fe_m, mitochondrial Fe, except for Fe found as nanoparticles; Fe_{mp}, nanoparticles found in mitochondria; Fe_n, cytosolic nanoparticles Fe; Fe_s, sensed Fe; HAADF, high-angle-annular-dark-field; HS, high-spin; IRP1 and IRP2, iron responsive element binding proteins 1 and 2, respectively; LS, low-spin; MB, Mössbauer; MIB, mitochondria isolation buffer; NHHS, non-heme high-spin; NTBI, non-transferrin-bound iron; OCR, oxygen consumption rate; ODE, ordinary differential equation; PBS, phosphate-buffered saline; Reg_-, surrogate for regulation in which increasing Fe_s inhibits; Reg_+, surrogate for regulation in which decreasing Fe_s stimulates; ROS, reactive oxygen species; STEM, scanning tunneling electron microscopy; TBI, transferrin-bound iron; TfRC1, transferrin receptor 1; $TfRC^+$, cells genetically modified to overexpress TfRC1; UTR, untranslated region; UV−vis, electronic absorption spectroscopy.

■ REFERENCES

(1) Anderson, G. J., and Vulpe, C. D. (2009) Mammalian iron transport. *Cell. Mol. Life Sci. 66*, 3241−3261.

(2) Hentze, M. W., Muckenthaler, M. U., Galy, B., and Camaschella, C. (2010) Two to Tango: Regulation of Mammalian Iron Metabolism. *Cell 142*, 24−38.

(3) Garrick, M. D., and Garrick, L. M. (2009) Cellular iron transport. *Biochim. Biophys. Acta 1790*, 309−325.

(4) Huebers, H., Josephson, B., Huebers, E., Csiba, E., and Finch, C. (1981) Uptake and release of iron from human transferrin. *Proc. Natl. Acad. Sci. U.S.A. 78*, 2572−2576.

(5) Tabuchi, M., and Kishi, F. (2000) Human NRAMP2/DMT1, Which Mediates Iron Transport across Endosomal Membranes, Is Localized to Late Endosomes and Lysosomes in HEp-2 Cells. *J. Biol. Chem. 275*, 22220−22228.

(6) Muckenthaler, M. U., Galy, B., and Hentze, M. W. (2008) Systemic Iron Homeostasis and the Iron-Responsive Element/Iron-Regulatory Protein (IRE/IRP) Regulatory Network. *Annu. Rev. Nutr. 28*, 197−213.

(7) Theil, E. C. (1987) Ferritin: Structure, Gene Regulation, and Cellular Function in Animals, Plants and Microorganisms. *Annu. Rev. Biochem. 56*, 289−315.

(8) Brissot, P., Ropert, M., Le Lan, C., and Loreal, O. (2012) Non-transferrin bound iron: A key role in iron overload and iron toxicity. *Biochim. Biophys. Acta 1820*, 403−410.

(9) Evans, R. W., Rafique, R., Zarea, A., Rapisarda, C., Cammack, R., Evans, P. J., Porter, J. B., and Hider, R. C. (2008) Nature of non-transferrin-bound iron: Studies on iron citrate complexes and thalassemic sera. *J. Biol. Inorg. Chem. 13*, 57−74.

(10) Hider, R. C. (2002) Nature of nontransferrin-bound iron. *Eur. J. Clin. Invest. 32*, 50−54.

(11) Jordan, I., and Kaplan, J. (1994) The mammalian transferrin-independent iron transport system may involve a surface ferrireductase activity. *Biochem. J. 302*, 875−879.

(12) Picard, V., Govoni, G., Jabado, N., and Gros, P. (2000) Nramp2 (DCT1/DMT1) Expressed at the Plasma Membrane Transports Iron and Other Divalent Cations into a Calcein-accessible Cytoplasmic Pool. *J. Biol. Chem. 275*, 35738−35745.

(13) Liuzzi, J. P., and Cousins, R. J. (2006) Zip14 (Slc39a14) mediates non-transferrin-bound iron uptake into cells. *Proc. Natl. Acad. Sci. U.S.A. 103*, 13612−13617.

(14) Oudit, G. Y., and Backx, P. H. (2003) L-type Ca^{2+} channels provide a major pathway for iron entry into cardiomyocytes in iron-overload cardiomyopathy. *Nat. Med. 9*, 1187−1194.

(15) Sohn, Y.-S., Ghoti, H., Breuer, W., Rachmilewitz, E. A., Attar, S., Weiss, G., and Cabantchik, Z. I. (2011) The role of endocytic pathways in cellular uptake of plasma non-transferrin iron. *Haematologica 97*, 670−678.

(16) Breuer, W., Ghoti, H., Shattat, A., Goldfarb, A., Koren, A., Levin, C., Rachmilewitz, E., and Cabantchik, Z. I. (2012) Non-transferrin bound iron in Thalassemia: Differential detection of redox active forms in children and older patients. *Am. J. Hematol. 87*, 55−61.

(17) Grootveld, M., Bells, J. D., Halliwell, B., Aruoma, O. I., Bomford, A., and Sadler, P. J. (1989) Non-transferrin-bound Iron in Plasma or Serum from Patients with Idiopathic Hemochromatosis. *J. Biol. Chem. 264*, 4417−4422.

(18) Bernstein, S. E. (1987) Hereditary hypotransferrinemia with hemosiderosis, a murine disorder resembling human atransferrinemia. *J. Lab. Clin. Med. 110*, 690−705.

(19) Valk, B. D., and Marx, J. J. M. (2000) Non-transferrin-bound iron is present in serum of hereditary haemochromatosis heterozygotes. *Eur. J. Clin. Invest. 30*, 248−251.

(20) SanMartín, C., Paula-Lima, A., Hidalgo, C., and Núñez, M. (2012) Sub-lethal levels of amyloid *β*-peptide oligomers decrease non-transferrin-bound iron uptake and do not potentiate iron toxicity in primary hippocampal neurons. *BioMetals*, 1−9.

(21) Baker, E., Baker, S. M., and Morgan, E. H. (1998) Characterisation of non-transferrin-bound iron (ferric citrate) uptake by rat hepatocytes in culture. *Biochim. Biophys. Acta 1380*, 21−30.

(22) Brissot, P., Wright, T. L., Ma, W. L., and Weisiger, R. A. (1985) Efficient Clearance of Non-transferrin-bound Iron by Rat Liver. *J. Clin. Invest. 76*, 1463−1470.

(23) Sturrock, A., Alexander, J., Lamb, J., Craven, C. M., and Kaplan, J. (1990) Characterization of a Transferrin-independent Uptake System for Iron in HeLa cells. *J. Biol. Chem. 265*, 3139−3145.

(24) Kaplan, J., Jordan, I., and Sturrock, A. (1991) Regulation of the Transferrin-independent Iron Transport System in Cultured Cells. *J. Biol. Chem. 266*, 2997−3004.

(25) Inman, R. S., and Wessling-Resnick, M. (1993) Characterization of Transferrin-independent Iron Transport in K562 Cells. *J. Biol. Chem. 268*, 8521−8528.

(26) Holmes-Hampton, G., Jhurry, N. D., McCormick, S. P., and Lindahl, P. A. (2013) Iron Content of *Saccharomyces cerevisiae* Cells Grown under Iron-Deficient and Iron-Overload Conditions. *Biochemistry 52*, 105−114.

(27) Miao, R., Holmes-Hampton, G., and Lindahl, P. A. (2011) Biophysical Investigation of the Iron in Aft1-1up and Gal-YAH1 *Saccharomyces cerevisiae*. *Biochemistry 50*, 2660−2671.

(28) Jhurry, N. D., Chakrabarti, M., McCormick, S. P., Holmes-Hampton, G., and Lindahl, P. A. (2012) Biophysical Investigation of the Ironome of Human Jurkat Cells and Mitochondria. *Biochemistry 51*, 5276−5284.

(29) Whitnall, M., Rahmanto, Y. S., Huang, M. L. H., Saletta, F., Lok, H. C., Gutiérrez, L., Lázaro, F. J., Fleming, A. J., Pierre, T. G. S., and Mikhael, M. R. (2012) Identification of nonferritin mitochondrial iron deposits in a mouse model of Friedreich ataxia. *Proc. Natl. Acad. Sci. U.S.A. 109*, 20590−20595.

(30) Stemmler, T. L., Lesuisse, E., Pain, D., and Dancis, A. (2010) Frataxin and mitochondrial FeS cluster biogenesis. *J. Biol. Chem. 285*, 26737−26743.

(31) Seguin, A., Sutak, R., Bulteau, A.-L., Garcia-Serres, R., Oddou, J.-L., Lefevre, S., Santos, R., Dancis, A., Camadro, J.-M., Latour, J.-M., and Lesuisse, E. (2010) Evidence that yeast frataxin is not an iron storage protein in vivo. *Biochim. Biophys. Acta 1802*, 531−538.

(32) Larrick, J. W., and Cresswell, P. (1979) Modulation of Cell Surface Iron Transferrin Receptors by Cellular Density and State of Activation. *J. Supramol. Struct. 11*, 579−586.

(33) Wiley, S. E., Rardin, M. J., and Dixon, J. E. (2009) Localization and function of the 2Fe-2S outer mitochondrial membrane protein MitoNEET. *Methods Enzymol. 456*, 233−246.

(34) Morales, J. G., Holmes-Hampton, G., Miao, R., Guo, Y., Münck, E., and Lindahl, P. A. (2010) Biophysical Characterization of Iron in Mitochondria Isolated from Respiring and Fermenting Yeast. *Biochemistry 49*, 5436−5444.

(35) Gohil, V. M., Sheth, S. A., Nilsson, R., Wojtovich, A. P., Lee, J. H., Perocchi, F., Chen, W., Clish, C. B., Ayata, C., Brookes, P. S., and Mootha, V. K. (2010) Nutrient-sensitized screening for drugs that shift energy metabolism from mitochondrial respiration to glycolysis. *Nat. Biotechnol. 28*, 249−255.

(36) Williams, J. M., Danson, D. P., and Janot, C. (1978) A Mössbauer determination of the iron core particle size distribution in ferritin. *Phys. Med. Biol. 23*, 835−851.

(37) Bovell, E., Buckley, C. E., Chua-anusorn, W., Cookson, D., Kirby, N., Saunders, M., and St. Pierre, T. G. (2009) Dietary iron-loaded rat liver haemosiderin and ferritin: *In situ* measurement of iron core nanoparticle size and cluster structure using anomalous small-angle X-ray scattering. *Phys. Med. Biol. 54*, 1209−1221.

(38) Bauminger, E. R., Harrison, P., Nowik, I., and Treffry, A. (1988) Composition and dynamics of iron in iron-poor ferritin. *Hyperfine Interact. 42*, 873−876.

(39) Miao, R., Martinho, M., Morales, J. G., Kim, H., Ellis, A., Lill, R., Hendrich, M. P., Münck, E., and Lindahl, P. A. (2008) EPR and Mössbauer Spectroscopy of Intact Mitochondria Isolated from Yah1p-Depleted *Saccharomyces cerevisiae*. *Biochemistry 47*, 9888−9899.

(40) Miao, R., Kim, H., Koppolu, M. K., Ellis, A., Scott, R. A., and Lindahl, P. A. (2009) Biophysical Characterization of the iron in mitochondria from Atm1p-depleted *Saccharomyces cerevisiae*. *Biochemistry 48*, 9556−9568.

(41) Campanella, A., Rovelli, E., Santambrogio, P., Cozzi, A., Taroni, F., and Levi, S. (2009) Mitochondrial ferritin limits oxidative damage regulating mitochondrial iron availability: Hypothesis for a protective role in Friedreich ataxia. *Hum. Mol. Genet. 18*, 1−11.

(42) Chen, W., Paradkar, P. N., Li, L., Pierce, E. L., Langer, N. B., Takahashi-Makise, N., Hyde, B. B., Shirihai, O. S., Ward, D. M., and Kaplan, J. (2009) Abcb10 physically interacts with mitoferrin-1 (Slc25a37) to enhance its stability and function in the erythroid mitochondria. *Proc. Natl. Acad. Sci. U.S.A. 106*, 16263−16268.

(43) Paradkar, P. N., Zumbrennen, K. B., Paw, B. H., Ward, D. M., and Kaplan, J. K. (2009) Regulation of Mitochondrial Iron Import through Differential Turnover of Mitoferrin 1 and Mitoferrin 2. *Mol. Cell. Biol. 29*, 1007−1016.

(44) Surovtsev, I. V., Morgan, J. J., and Lindahl, P. A. (2007) Whole-cell modeling framework in which biochemical dynamics impacts aspects of cellular geometry. *J. Theor. Biol. 231*, 581−596.

(45) Seguin, A., Santos, R., Pain, D., Dancis, A., Camadro, J.-M., and Lesuisse, E. (2011) Co-precipitation of phosphate and iron limits mitochondrial phosphate availability in *Saccharomyces cerevisiae* lacking the Yeast Frataxin Homologue (*YFH1*). *J. Biol. Chem. 286*, 6071−6079.

(46) Pandolfo, M., and Pastore, A. (2009) The pathogenesis of Friedreich ataxia and the structure and function of frataxin. *J. Neurol. 256*, 9−17.

(47) Lu, C., and Cortopassi, G. (2007) Frataxin knockdown causes loss of cytoplasmic iron-sulfur cluster functions, redox alterations and induction of heme transcripts. *Arch. Biochem. Biophys. 457*, 111−122.

(48) Shaw, G. C., Cope, J. J., Li, L., Corson, K., Hersey, C., Ackermann, G. E., Gwynn, B., Lambert, A. J., Wingert, R. A., Traver, D., Trede, N. S., Barut, B. A., Zhou, Y., Minet, E., Donovan, A., Brownlie, A., Balzan, R., Weiss, M. J., Peters, L. L., Kaplan, J., Zon, L. I., and Paw, B. (2006) Mitoferrin is essential for erythroid iron assimilation. *Nat. Lett. 440*, 96−100.

(49) Nandal, A., Ruiz, J. C., Subramanian, P., Ghimire-Rijal, S., Sinnamon, R. A., Stemmler, T. L., Bruick, R. K., and Philpott, C. C. (2011) Activation of the HIF Prolyl Hydroxylase by the Iron Chaperones PCBP1 and PCBP2. *Cell Metab. 14*, 647−657.

(50) Shi, H., Bencze, K. Z., Stemmler, T. L., and Philpott, C. C. (2008) A Cytosolic Iron Chaperone That Delivers Iron to Ferritin. *Science 320*, 1207−1209.

(51) Rothen, A. (1944) Ferritin and Apoferritin in the ultracentrifuge. *J. Biol. Chem. 152*, 679−693.

(52) Dickson, D. P. E., Reid, N. M. K., Mann, S., Wade, V. J., Ward, R. J., and Peters, T. J. (1988) Mössbauer spectroscopy, electron microscopy and electron diffraction studies of the iron cores in various human and animal haemosiderins. *Biochim. Biophys. Acta 957*, 81−90.

(53) Macara, I. G., Hoy, T. G., and Harrison, P. M. (1972) The formation of ferritin from apoferritin: Kinetics and mechanism of iron uptake. *Biochem. J. 126*, 151−162.

(54) Crichton, R. R., and Paques, E. (1977) A kinetic study of the mechanism of ferritin formation. *Biochem. Soc. Trans. 5*, 1130−1131.

(55) St. Pierre, T. G., Tran, K. C., Webb, J., Macey, D. J., Pootrakul, P., and Dickson, D. P. E. (1992) Core structures of haemosiderins deposited in various organs in *β*-thalassemia/Haemoglobin E disease. *Hyperfine Interact. 71*, 1279−1282.

(56) Bell, S. H., Weir, M. P., Dickson, D. P. E., Gibson, J. F., Sharp, G. A., and Peters, T. J. (1984) Mössbauer spectroscopic studies of human haemosiderin and ferritin. *Biochim. Biophys. Acta 787*, 227−236.

(57) Michel, F. M., Hosein, H.-A., Hausner, D. B., Debnath, S., Parise, J. B., and Strongin, D. R. (2010) Reactivity of ferritin and the structure of ferritin-derived ferrihydrite. *Biochim. Biophys. Acta 1800*, 871−885.

(58) Hartwig, A., and Schlepegrell, R. (1995) Induction of oxidative DNA damage by ferric iron in mammalian cells. *Carcinogenesis 16*, 3009.

(59) Hartwig, A., Klyszcz-Nasko, H., Schlepegrell, R., and Beyersmann, D. (1993) Cellular damage by ferric nitrilotriacetate and ferric citrate in V79 cells: Interrelationship between lipid peroxidation, DNA strand breaks and sister chromatid exchanges. *Carcinogenesis 14*, 107−112.

(60) Ingraham, L. L., and Meyer, D. L. (1985) Catalases and Peroxidases. In *Biochemistry of Dioxygen*, 1st ed., pp 91−105, Plenum Press, New York.

(61) Ames, B. N., Shigenaga, M. K., and Hagen, T. M. (1993) Oxidants, antioxidants, and the degenerative diseases of aging. *Proc. Natl. Acad. Sci. U.S.A. 90*, 7915−7922.

(62) Cockrell, A. L., Holmes-Hampton, G. P., McCormick, S. P., Chakrabarti, M., and Lindahl, P. A. (2011) Mössbauer and EPR Study of Iron in Vacuoles from Fermenting *Saccharomyces cerevisiae*. *Biochemistry 50*, 10275−10283.